DEM-based modelling framework for spray-dried powders in ceramic tiles industry. Part I: Calibration procedure

J.M. Tiscar, A. Escrig, G. Mallol, J. Boix, F.A. Gilabert

PII: S0032-5910(19)30652-7
DOI: https://doi.org/10.1016/j.powtec.2019.08.053
Reference: PTEC 14613

To appear in: *Powder Technology*

Received date: 2 May 2019
Revised date: 2 August 2019
Accepted date: 20 August 2019

Please cite this article as: J.M. Tiscar, A. Escrig, G. Mallol, et al., DEM-based modelling framework for spray-dried powders in ceramic tiles industry. Part I: Calibration procedure, Powder Technology, https://doi.org/10.1016/j.powtec.2019.08.053

DEM-based modelling framework for spray-dried powders in ceramic tiles industry. Part I: calibration procedure.

J.M. Tiscar[a,*], A. Escrig[a], G. Mallol[a], J. Boix[a], F.A. Gilabert[b]

[a]*Instituto de Tecnología Cerámica (ITC) – Universidad Jaume I (UJI), Castellón; Spain*

[b]*Department of Materials, Textiles and Chemical Engineering, Faculty of Engineering and Architecture, Ghent University (UGent). Tech Lane Ghent Science Park - Campus A, Technologiepark-Zwijnaarde 46, B-9052 Zwijnaarde (Ghent); Belgium.*

Abstract

This work describes a combined experimental-numerical study to characterize fine spray-dried powder used in the ceramic tile pressing process. A DEM-based granular assembly is endowed with a new set of scaling laws that allows for simulating reliably industrial processes using a much lower number of granules. To do it, a calibration strategy relying on three experimental setups is proposed; (i) compression test of bulk for granule stiffness, (ii) dynamic angle of repose and (iii) image analysis of the powder motion in a rotating drum for the intergranular and granular-boundary sliding and rolling friction coefficients. In order to evaluate the powder motion in a rotating drum, a robust method relying on a direct image analysis is proposed. This methodology makes it possible to quantitatively assess the frictional properties of the powder in contact with different surface materials.

Keywords: spray-dried powder, rotating drum angle of repose, calibration, discrete element method, scaling-up

1. Introduction

The procedure of forming ceramic tiles basically consists of three stages: first, the powder is poured in a mould via a transportation system, secondly it is compacted using a uniaxial hydraulic press and finally, the generated “green tile” is moved to a kiln for the firing stage [1, 2].

---

[*] Corresponding author. Phone: +34678070851

Email address: `juanmiguel.tiscar@itc.uji.es` (J.M. Tiscar)

Despite the important advances in pressing systems and kiln technology, interestingly, the first stage of filling has not experienced progress over the past few decades [3]. Nowadays, the accuracy of this stage still relays on the experience and intuition of the operator, being this particularly relevant when it comes to fabricating large tile formats (up to 120 cm x 120 cm). Despite the operator's skills, this is a procedure that is still greatly prone to generating defects in the tiles due to a poor powder distribution in the mould [4]. In the authors' opinion, there is still a lack of a scientifically-based and systematic approach to improve this stage. In this regard, DEM simulations depict a suitable computational approach to analyse how these defects are generated during the forming of ceramic tiles as well as to propose the strategy to prevent or minimize them. This work is the first of a series of three papers that present a combined numerical-experimental framework based on DEM simulations to understand and improve the mould filling stage currently employed in the ceramic tile industry.

The Discrete Element Method (DEM) is a well-established computational technique to simulate different movement regimes of granular materials. This method was first proposed by Cundall and Strack [5]. Later on, Luding [6] extended the physical model, including rolling and torsion resistance [7], analogous to the sliding friction model. Concerning the scalability, Sakai et al. [8] introduced the coarse granule model in order to simulate realistic industrial scenarios, where the amount of involved particles leads to unaffordable computations.

DEM has been used in the analysis of powder flow during silo discharge [9], filling and packing particles [10], segregation studies [11, 12], in the simulation of compression test [13] or in the mixing and transport of powders [14]. In the pharmaceutical industry, DEM has demonstrated the influence of filling cadence and die form in powder segregation [15]. In addition, recent studies [16] have shown that die filling with complex shapes can be successfully simulated using DEM with a simple linear model and the signed distance function as wall boundary.

In order to set the model parameters, a calibration procedure is required. Calibration consists in setting the model parameters through reproduction of real experiments. These parameters are selected so that certain simulated macroscopic magnitudes compare correctly with the experimental results. In this point, there is still a lack of sufficient benchmarks to validate DEM simulations under industrial environments [17]. Some efforts have been done to settle a robust calibration procedure [18, 19], where the ambiguity of parameter combination was addressed. Recently, probabilistic [20] and rheometric [21] based calibrations have also been performed, and a review of the calibration procedures can be found in [22], where the existing variety of calibration studies is shown. Nevertheless, the morphology and particle size of the powder ultimately determine the calibration testing setup (due to the computational limits and the required small time increment), and in most cases the multiple parameters involved in the constitutive laws and the assumed simplifications lead to design custom calibration tests according to specific applications and conditions [23]. To the best of authors' knowledge and experience, some sectors like those related to ceramic tile production are currently demanding a straightforward calibration procedure, where micrometric granules with a wide granule size distribution are involved. The current state of the art is lacking of a robust and reliable framework to calibrate DEM models. In that sense, this calibration framework to simulate an industrial process must be straightforward in terms of implementability, namely, the costs involved in the experimental setup arrangement and test execution time of the material parameter identification must be as low as possible.

In DEM, the most widely used model to describe the powder dynamics is the linear spring-dashpot (LSD) model [5]. To calibrate the LSD model, confined axial compression tests [18, 24, 17] and shear cell tests [25, 26] are widely used, where intergranular stiffness and friction coefficients can be assessed, respectively. The shear cell test is suitable for coarse materials, such as corn [10] or polyethylene pellets [1], with granules of millimeter size. Unfortunately, when finer granules are involved (≤ 1 mm), the shear cell test simulation is computationally unfeasible if real properties are used [27, 28]. As the granule size decreases, not only the number of granule increases, but a smaller integration time step is required to simulate successfully the calibration procedure without adding numerical artifacts. For example, Coetzee et al [18] showed a DEM calibration using the direct shear cell with relatively large particles. However, O'Sullivan et al [26] found that when small particles are involved, stability issues (a consequence of the small particle masses in comparison with the contact stiffnesses) and some discrepancies between the real and simulated tests arise, i.e., in the values of the angle of friction and normal stresses obtained from a direct shear cell test.

Another issue associated with the shear tests is the required time to perform a full test, because the longer the elapsed time to perform a test, the longer the simulation. Table 1 shows the estimated time to perform typical tests used to calibrate DEM parameters with different equipments, including the angle of repose test used in this paper. The pre-conditioning step, which is usually applied to remove the packing history of the powder, is not considered (it is normally ignored in the simulations to reduce the computational cost). The dynamic angle of repose is the shortest test, followed by the FT4 rheometer test. The shear cell test can be significantly longer compared to the others. Regarding the FT4, which is a universal powder rheometer, the typical full test duration takes a few minutes but only short cycles are simulated. The confined compression test is also a long test, but no better alternatives to calibrate the stiffnesses have been found in the literature.

This study presents an alternative, faster and straightforward methodology to calibrate powder models composed of granules with a wide range of sizes. The methodology also relies on scaling laws that make it possible to study big granular assemblies typically used in powder-based industrial applications.

This paper is organized as follows: section 2 presents the numerical model used to simulate the powder and the scaling laws. Section 3 addresses the experimental part of this work, where the powder material and the setups used to calibrate the model are described. The rolling and sliding friction coefficients of intergranular and granule-boundary were determined using a rotating drum. With it, measurements of dynamic angles of repose and powder dynamics can be achieved. Section 4 presents the details of the identification parameter process and the results of the calibration. The influence of using different types of wall surface in the powder response is also addressed. This paper concludes by summarizing the main findings as well as the limitations and basic assumptions required for this type of analysis. Additionally, two appendices are included dealing with the computational validation of the used DEM framework. 7 shows the verification of the implemented constitutive equations for the contact law (Scilab script is provided as Supplementary Material) and 8 presents the study of scaling independence. Further details of validation by simulating real mould filling industrial processes will be presented in a forthcoming publication.

2. Theory

2.1. *Model formulation*

The LSD model [6] was selected due to its well-balanced ratio between simplicity from the computational point of view and reliability of its response from the physical point of view. Despite its simplicity, this model has proved efficient and accurate to simulate the powder dynamics [29, 30, 31] and powders under low consolidation stresses [32, 33]. Its development results in the well-known differential equation of the damped harmonic oscillator.

Fig. 1 shows schematically of the forces involved in the interaction between granules. When two spherical particles, *i* and *j* (with diameters d_i and d_j, respectively) are close to each other, they can collide generating a force $\mathbf{F}_{ij}$ and a moment $\mathbf{\Gamma}_{ij}$ on the contact point. The collision occurs when there is an interpenetration between the particles. The interpenetration value is defined as $h_{ij} = R_i + R_j - \| \mathbf{r}_i - \mathbf{r}_j \|$, where $\mathbf{r}_i$ and $\mathbf{r}_j$ are the position of the particles center and R_i and R_j are the radii of the particles i and j, respectively.

A granular system is modelled as a set of spatial coordinates $\mathbf{r}_i$ and angular coordinates $\boldsymbol{\theta}_i$ with $i = 1, \ldots, N_p$, where N_p is the total number of particles in the system. The time evolution of these quantities is governed by:

$$m_i \frac{d^2 \mathbf{r}_i}{dt^2} = \sum_j^{N_c} \mathbf{F}_{ij} + m_i \mathbf{g} \tag{1}$$

$$I_i \frac{d^2 \boldsymbol{\theta}_i}{dt^2} = \sum_j^{N_c} \mathbf{\Gamma}_{ij} \tag{2}$$

In these equations, the summation is extended to the N_c particles (or surfaces) in contact with the particle *i*. m_i and I_i are the mass and moment of inertia, respectively, and $\mathbf{g}$ is the gravity. In this work, adhesive forces are not considered. Moments occurring in (2) are due to tangential and rolling forces.

In the LSD model, the contact forces $\mathbf{F}_{ij,n}$ and $\mathbf{F}_{ij,s}$, which are the normal and tangential forces between two particles, can be formulated as:

$$\mathbf{F}_{ij,n} = -k_{\mathrm{n}} h_{ij} \mathbf{n}_{ij} - \gamma_{\mathrm{n}} \mathbf{v}_{rel,n} \tag{3}$$

$$\gamma_{\mathrm{n}} = \begin{cases} 2\xi \sqrt{m^* k_{\mathrm{n}}} & if \quad \mathbf{v}_{rel,n} \cdot \mathbf{n}_{ij} < 0 \\ 0 & if \quad \mathbf{v}_{rel,n} \cdot \mathbf{n}_{ij} > 0 \end{cases} \tag{4}$$

$$\mathbf{v}_{rel,n} = ((\mathbf{v}_i - \mathbf{v}_j) \cdot \mathbf{n}_{ij}) \times \mathbf{n}_{ij} \tag{5}$$

$$\mathbf{F}_{ij,s}^{(t)} = \mathbf{F}_{ij,s}^{(t-\Delta t)} - k_{\mathrm{s}} \Delta\delta_s \Delta\delta_s = \mathbf{v}_{rel,s} \Delta t \tag{6}$$

$$\begin{aligned}\mathbf{v}_{rel,s} &= (\mathbf{v}_i - \mathbf{v}_j) - ((\mathbf{v}_i - \mathbf{v}_j)\cdot \mathbf{n}_{ij})\mathbf{n}_{ij} \\ &+ (R_i\omega_i + R_j\omega_j)\times \mathbf{n}_{ij}\end{aligned} \tag{7}$$

$$\begin{aligned}\mathbf{F}_{ij,s} &= \mu_s \|\mathbf{F}_{ij,n}\| \frac{\mathbf{F}_{ij,s}}{\|\mathbf{F}_{ij,s}\|} \\ \text{if} \quad &\|\mathbf{F}_{ij,s}\| > \mu_s \|\mathbf{F}_{ij,n}\|\end{aligned} \tag{8}$$

The superscript t denotes the current time and Δt is the time step. The reduced mass m^* is calculated as $m^* = m_i m_j / (m_i + m_j)$, k_n and k_s are the normal and tangential spring elastic constants, γ_{n} is the normal viscous damping and ξ is the damping ratio. Note that the tangential viscous damping was not considered. $\Delta\boldsymbol{\delta}_s$ is the corresponding increment of the tangential overlap; $\mathbf{n}_{ij} = (\mathbf{r}_j - \mathbf{r}_i)/\|\mathbf{r}_j - \mathbf{r}_i\|$ is the normal unit vector pointing from particle i to particle j, $\mathbf{v}_{rel,n}$ and $\mathbf{v}_{rel,s}$ represent the relative normal and tangential velocities between two particles, and $\mathbf{v}_i$ and $\mathbf{v}_j$ are the velocities of the particles i and j, respectively. Finally, $\boldsymbol{\omega}_i$ and $\boldsymbol{\omega}_j$ are the angular velocities for each particle, and μ_s is the sliding friction coefficient.

The torques between two particles, $\boldsymbol{\Gamma}_{ij}$ and $\boldsymbol{\Gamma}_{ji}$ are defined as:

$$\boldsymbol{\Gamma}_{ij} = R_i \mathbf{n}_{ij} \times \mathbf{F}_{ij,s} - R^* \mathbf{n}_{ij} \times \mathbf{F}_{ij,r} \tag{9}$$

$$\boldsymbol{\Gamma}_{ji} = R_j \mathbf{n}_{ij} \times \mathbf{F}_{ij,s} + R^* \mathbf{n}_{ij} \times \mathbf{F}_{ij,r} \tag{10}$$

The reduced radius R^* is calculated as $R^* = R_i R_j / (R_i + R_j)$. The rolling quasi-force $\mathbf{F}_{ij,r}$, is defined as:

$$\mathbf{F}_{ij,r}^{(t)} = \mathbf{F}_{ij,r}^{(t-\Delta t)} - k_r \Delta\boldsymbol{\delta}_r \Delta\boldsymbol{\delta}_r = \mathbf{v}_{rel,r}\Delta t \tag{11}$$

$$\mathbf{v}_{rel,r} = -R^*(\boldsymbol{\omega}_i - \boldsymbol{\omega}_j) \times \mathbf{n}_{ij} \tag{12}$$

$$\begin{aligned}\mathbf{F}_{ij,r} &= \mu_r \|\mathbf{F}_{ij,n}\| \frac{\mathbf{F}_{ij,r}}{\|\mathbf{F}_{ij,r}\|} \\ \text{if} \quad &\|\mathbf{F}_{ij,r}\| > \mu_r \|\mathbf{F}_{ij,n}\|\end{aligned} \tag{13}$$

$\Delta\boldsymbol{\delta}_r$ is the increment of the rolling overlap, k_r represents the rolling spring elastic constant, $\mathbf{v}_{rel,r}$ represents the objective relative rolling velocity between two particles, and μ_r is the rolling friction coefficient.

Newton's third law is applied in order to enforce the correct force direction for each particle. The boundary surfaces were considered to be granules of infinite mass, infinite radius, and infinite normal stiffness. It is important to note that the directions of the tangential force and the rolling quasi-force from the previous time step $\mathbf{F}^{(t-\Delta t)}$ must be corrected at the new time step [7]. Additionally, the Coulomb criterion (Eqs. (8) and (13)) is applied to truncate the tangential force and the rolling quasi-force with the maximal possible value, i.e. the product of the friction coefficient and the magnitude of the normal contact force. For further details, see [7, 32]. In this work the Verlet integration scheme [34] was used, and the time increment Δt must be smaller than the critical time increment in order to guarantee numerical stability. For the LSD model, the critical time step [35] is defined as:

$$\Delta t_{crit} = \sqrt{\frac{m}{k_n}} \tag{14}$$

where m is the mass of the lightest granule and k_n is the normal spring elastic constant. In this work, the selected time step was $0.6\Delta t_{crit}$.

2.2. Scaling laws

The computational cost of DEM simulations increases with the number of particles in the system. Unfortunately, many industrial processes of interest typically involve a huge number of particles (more than 10 millions) which cannot be simulated even using the highest current computational resources. For this reason, the application of scaling laws is essential to reduce the number of particles in the system with the aim of simulating industrial processes realistically. To do this, the coarse granule model approach is widely used [8, 36]. In this scaling method, the number of particles is reduced by increasing their size, but trying to keep the overall dynamic response unaltered. Recently, Lommen et al. [37] presented another approach of the coarse granule model, which is applied to the Hertz physical model. This novel approach conserves the character of the contact, making it possible to scale correctly particle assemblies. The scaling laws proposed in the present work are fundamentally based in the coarse granule model proposed by Hilton et al. [36].

A real system with N^r particles can be reduced to N^s particles using the following equation:

$$\lambda = \frac{N^r}{N^s} = \frac{V^s}{V^r} = \left(\frac{R^s}{R^r}\right)^3 \tag{15}$$

where λ is the scale factor, V and R stand for the volume and radius of the particle, respectively, and the superscripts “r” and “s” refer to “real” and “scaled” variables, respectively. One way to apply the coarse grain model is to keep the mass of the coarse granule constant. In that case, the following relation must hold:

$$m = \rho^r V^r = \rho^s V^s \tag{16}$$

where ρ is the density of the particle. Comparing Eq. (15) with Eq. (16), the following relationship can be obtained:

$$\frac{\rho^s}{\rho^r} = \lambda^{-1} \tag{17}$$

This expression corrects the density of every particle when their volumes change, what leads to the same coarse granule model approach presented by Hilton et al. [36]. Notice that this way enables us to obtain the coarse granule model by changing just the size of the granules and its density.

Another scaling law must be applied in order to keep constant the average coordination number in the system. As it can be observed in the Fig. 2, when the particle size increases while keeping its mass unaltered, the relative overlap (defined as h_{ij} / R) will decrease, which in turn might decrease the coordination number.

In order to keep the relative overlap constant, the relationship between λ and the stiffness coefficient k_n is:

$$\frac{k_n^s}{k_n^r} = \frac{R^r}{R^s} = \lambda^{-1/3} \tag{18}$$

Therefore, two scaling laws are required to obtain an appropriate similarity between the scaled and the real system.

Nevertheless, the scale factor cannot be increased indefinitely and, for each application, it is necessary to determine the minimum number of particles that reproduce the studied effect, since its influence in some experiments, like the angle of repose tests, has been proved [38, 39]. This situation would be analogous to what happens during the process of mesh convergence required in simulations based on finite element method. Therefore, when this type of scaling is applied, a preliminary analysis is crucial to determine the maximum applicable scale factor (Appendix B).

3. Experimental procedures

3.1. *Spray-dried powder characterization*

A standard porcelain tile powder (Grupo EUROATOMIZADO®) was selected. The powder was dried to avoid cohesion effects due to moisture presence, which ranges between 4 and 8 % on a dry basis. Drying was performed in a laboratory oven at 110 °C for 24 hours. A sieve analysis was used to extract the granule size distribution (GSD) of the spray-dried powder. Fig. 3 shows the granule morphology and the GSD. It can be observed that the spray-dried powder is quite spherical, therefore, it was considered appropriate to approximate the shape of the granules to perfect spheres. The density of the granules was measured in laboratory tests, estimating an average value of 1800 kg/m^3. The GSD was fitted to a log-normal distribution with a number-median distribution of 200 µm and a geometric deviation of 1.43.

3.2. *Calibration strategy*

Calibration is necessary to approximate the rheological behaviour of simulated powder to the real one. Several experiments were selected to calibrate the model, which ideally should maximize the influence of one or two parameters and minimize the others. They should be short experiments, because DEM simulations require a high computational effort to simulate the necessary amount of particles with small time steps for numerical stability. Despite the use of scaling laws, the simulated macroscopic properties are usually *not* independent of the scaling factor, therefore, this factor must be reduced until convergence is achieved. Furthermore, experiments must be reproducible. It is worth mentioning that the calibration procedure outlined in this section is intentionally aimed at being straightforward, flexible and computationally less demanding. Therefore, although more complex calibration strategies can be found in [23, 18, 19], they rarely deal with small particles (<1 mm) which are relatively common in industrial scenarios and they imply a much higher computational effort, scaling laws and a high variability of the material properties.

For the sake of simplicity, in all simulations the three types of stiffnesses were assumed to be equal to each other ($k_n = k_s = k_r$) and the damping coefficient was set to 70 % of the critical damping coefficient, assuming quasi-static conditions [9].

First, the confined compression test was used to evaluate the granule stiffness value. Next, the measurement of the dynamic angle of repose and the powder motion inside a rotating drum was performed to find the corresponding values for the friction coefficients. These friction coefficients are four: the sliding and rolling friction coefficients between granules ($\mu_{s,g-g}$ and $\mu_{r,g-g}$) and the sliding and rolling friction coefficients between the granules and the boundary ($\mu_{s,g-s}$ and $\mu_{r,g-s}$). All tests were recorded with a video capture system. A color digital Camera (Canon PowerShot S90) was used for image acquisition. The camera was attached to a tripod completely perpendicular to the ground.

3.2.1. *Confined compression test*

To determine the stiffnesses, compression tests were quasistatically conducted at low pressures [9, 24]. A vertical load is applied to the bulk powder confined in a cylindrical container and the bulk material is compressed along the vertical axis. Bulk material strain is associated with the stiffness parameter in DEM simulations.

Fig. 4 shows the equipment used to perform the test. A universal Instron testing machine was used with a cylindrical die that contained the bulk material. This die had an inner diameter of 76 mm and a depth of 15 mm. The spray-dried powder was subjected to several compression-decompression cycles between a maximum and minimum pressure until a pseudo-steady state was achieved. The normal load and resulting axial displacement were recorded and the normal stress and strain (σ and ε , respectively) were calculated. During the first cycles a rearrangement of particles took place, and as a result the cycles were not stable. This was because the packing was not perfect and intergranular movements occurred in this stage. However, in the last cycles when the particle movement was limited, stable hysteresis loops were obtained. Confined Young's modulus E' , obtained from stable cycles, can be calculated as:

$$E' = \frac{\sigma_{max} - \sigma_{min}}{\varepsilon_{max} - \varepsilon_{min}} \tag{19}$$

where σ_{max} is the maximum axial compression stress, ε_{max} is its associated strain, σ_{min} the minimum axial compression stress and ε_{min} its associated strain.

The pressure limits of the compression cycles were selected in a series of preliminary trials such that, at maximum pressure, no breakage of the spray-dried granules occurred, whilst at minimum pressure the granules were still in direct contact with each other.

The load application rate was very low (1 mm/min). Consequently, the test was conducted under quasi-static conditions implying that the forces were exclusively governed by the intergranular elastic contacts.

3.2.2. Dynamic angle of repose

The dynamic angle of repose or flowing angle is a widely used measure for the flowability characterization of powders by using rotating drums [40, 41].

The equipment for measuring the dynamic angle of repose is shown in Fig. 5. The assembly consists of a rotating drum and a variable DC power supply in order to control the drum rotational speed. The drum was constructed with polycarbonate and had an inner diameter of 100 mm and a depth of 44 mm. The powder was inserted into the drum through a movable end plate. Moreover, sheets of different materials were prepared to cover the inner drum wall in order to analyse the motion and the dynamic angle of repose with different wall materials. In this test, the rotation rate remained constant at 4 rpm with a filling degree of 43 %, which produced a rolling motion with a steady flow. In this type of motion, the dynamic angle of repose can be measured as the angle formed between the horizontal and the inclined plane formed by the particles.

The dynamic angle of repose was determined through the open source image processing software ImageJ [42]. The same procedure was used for both experimental and simulated results.

3.2.3. The area method

The aforementioned rotating drum can be used to obtain more valuable information about the powder, as for example how the powder motion occurs into the drum at different rotational speeds. With this purpose, an additional methodology called “the area method” is presented here to achieve the powder calibration. The area method consists in tracking the evolution of the cross-sectional area (CSA) of the drum occupied by the powder as a function of the rotational speed of the drum. It must be noticed that the higher the rotational speed, the higher the CSA of the drum occupied by the powder, until centrifugation occurs. Likewise, as long as centrifugation does not occur, the higher the CSA of the drum occupied by the powder, the higher the porosity of the powder bed. In this test the filling degree was also 43 %.

This method brings two advantages over other calibration tests such as the static angle of repose [43, 44, 45]: firstly, the methodology is fast, because the physical simulation time takes less than 3 seconds; second, this calibration test is purely dynamic, and therefore very suitable to calibrate the powder models undergoing highly dynamic situations (very common for DEM simulations aimed at industrial environments).

In this test, 5 different rotational speeds for the area method were studied: 4, 40, 80, 105 and 116 rpm, which cover a wide range of speeds. Fig. 6 shows the evolution of the powder flow in the drum for every rotation speed.

Fig. 7b shows a red circumference, that encloses the area corresponding to the CSA of the drum (CSA_{drum}), and a black area corresponds to the CSA occupied by the powder. Therefore, the CSA occupied by the powder (CSA_{oc}) can be obtained by the following relationship:

$$\mathrm{CSA_{oc}}(\%) = 100\,\frac{\mathrm{blackarea(units)}}{\mathrm{CSA_{drum}(units)}} \tag{20}$$

3.3. *Preparing the cylindrical surfaces*

In order to evaluate the coefficients of friction of the granules with different surfaces, cylindrical plates of different materials were collected. Fig. 8 shows four different cylindrical surfaces made of aluminium, polypropylene (PP), polytetrafluoroethylene (PTFE) and granules. Fig. 9 shows a zoomed view of the surface covered by granules.

Among all surfaces, the surface coated with granules has a great interest because it makes possible to obtain the intergranular friction coefficients. The preparation consisted in covering one side of a plastic surface with double-face adhesive tape. Then, the porcelain tile powder was sprinkled over the surface. Finally, the surface was vibrated to homogenize and spread the granules uniformly.

This coating of granules neutralizes the effect of the plastic inner surface of the drum on the behaviour of the powder, in such a way that each granule always interacts with another granule. For the sake of simplicity, it is assumed that in this drum the inner surface has a major impact on the powder motion than the end plates. Notice that some researchers have identified that, depending on the diameter to depth ratio of the drum, the end plates can exhibit a significant influence on the powder dynamics [46, 47].

3.4. *Simulation details*

The DEM simulations were performed on an in-house software developed. The software was implemented using the C++ programming language. A brief computational verification of the software is included in Appendix A, which will be extended in a forthcoming paper. Numerical simulations were performed on a cluster with 2 Intel Xeon hexacore E5649 2.53 GHz processors and 48 GB of RAM memory. The operating system was CentOS 6. The code was compiled using g++ 5.2 with the compiler flag -Ofast.

4. Results and discussion

4.1. Determination of the stiffnesses

The stiffness of the granules showed in Fig. 3 was determined using the confined compression test described in section 3.2.1. Fig. 10 presents the experimental and numerical force-displacement curves. The first cycle produces a wider deformation range of the granular bed in comparison to the subsequent cycles. This situation is a result of the rearrangement regime of granules. It can be seen that the deformation increases slightly in every applied cycle, until reaching a stationary state. Once the granular assembly reaches this level of packing, the level of permanent deformation does not increase by applying additional cycles. This means that the deformation produced within a stationary cycle is mostly elastic, and therefore, it should be related to the Young's modulus of the granules. After 3 repetitions, the confined Young's modulus was obtained from the stationary compression cycle. An average value of 45.4 ± 1.5 MPa was measured for the dry spray-dried powder.

This compression experiment was simulated using DEM as described in section 2. A total of six simulations were performed, in which the value of the stiffness was changed between 250 up to 10000 N/m. Fig. 10 shows the curves resulting from the simulations using two extreme stiffnesses. This response agrees very well with the results from other authors [24]. It can be seen that using granules with higher stiffness, the compressibility of the granular assembly decreases accordingly. For all the confined compression test simulations the scale factor was $\lambda = 27$, simulating a total of 62000 granules. The influence of the intergranular friction coefficients is negligible during this type of test [9]. However, the effect of the granule-boundary frictions had to be considered in the simulations because the friction of the granules with the lateral surface of the cylinder has a certain influence in the resulting force-displacement curves. In fact, it has been demonstrated that increasing the value of the sliding friction coefficient between the granules and surfaces contributes to a stiffening of the system [47, Chapter 5]. Taking this into account, as a first approximation the wall friction coefficients were set to 0.2 (both a significantly low values).

Fig. 11 shows the confined Young’s modulus of the granular bulk versus the stiffness of the granules used in the simulations. The extrapolation of the simulation results indicates that the stiffness required to obtain the experimental confined Young’s modulus (45.4 MPa) should be 87000 N/m. The simulation of the studied powder with this granule stiffness involves a critical time step of 10^{-7} s. At present, this time step hinders a practical usage of the model for real industrial scenarios, even if the most powerful computational resources are employed. A different strategy was finally followed: the stiffness value was set to the minimum value that keeps the coordination number constant during the filling of a graduated cylinder. This was deemed appropriate given the dominant role of the collisional regime in the target applications. During this type of regime only small strains (or overlappings) are expected [32].

To determine the smallest but acceptable stiffness constant, a series of 14 DEM simulations were performed using different stiffnesses values. The granules were poured in a metallic cylindrical container with a diameter of 100 mm and a depth of 40 mm (without applying the compression cycles) and the evolution of the average coordination number was analysed. All these simulations were made with a scale factor of $\lambda = 125$ and 80000 granules. Fig. 12 shows the coordination number obtained when the granules are in steady state, as a function of the stiffness value. The results of this test are consistent with those from Ref. [48]. For stiffness values lower than 200 N/m a excessively high coordination number variation is retrieved. However, for values greater than 200 N/m, the coordination number hardly changes. As a result, a stiffness of 200 N/m was proposed because lower stiffnesses produce bigger time steps and it drastically reduces the computational cost of the simulations.

This assumption implies that the results obtained in systems where the intergranular compressive response plays an important role might not be realistic [29]. Nevertheless, it is expected that the external forces acting on certain applications, like powder dynamics, are small [49, 50]. In fact, according with the results observed in Fig. 12, Loomen et al [48] showed that a stiffness reduction can be applied without altering the simulation results as long as only low external forces are involved. However, this reduction should be made cautiously and the model results need to be thoroughly verified against different benchmarks.

4.2. Determination of the intergranular friction coefficients

To determine the intergranular friction coefficients ($\mu_{s,g-g}$ and $\mu_{r,g-g}$), the dynamic angle of repose test and the area method were performed. It was assumed that granule-boundary friction coefficients ($\mu_{s,g-s}$ and $\mu_{r,g-s}$) of the surfaces covered with granules are identical to $\mu_{s,g-g}$ and $\mu_{r,g-g}$, respectively. This assumption reduces the number of unknowns to only two, $\mu_{s,g-g}$ and $\mu_{r,g-g}$. Therefore, the problem consists in finding pairs of $\mu_{s,g-g}$ and $\mu_{r,g-g}$ that simultaneously reproduce the dynamic angle of repose and the evolution of the area occupied by the powder in the rotating drum.

The strategy to obtain the intergranular friction coefficient was the following:

1. Determine pairs of $\mu_{s,g-g}$ and $\mu_{r,g-g}$ which reproduce the dynamic angle of repose.
2. Perform the simulations of the area method with pairs of $\mu_{s,g-g}$ and $\mu_{r,g-g}$ obtained previously.
3. Select the pair of values that best reproduces the area method.

Using the surfaces coated with granules, the experimental dynamic angle of repose was 34.6°. Several simulations of the dynamic angle of repose were performed using a range of sliding and rolling friction coefficients (Fig. 13). The number of simulated granules was 200000, with a scale factor of $\lambda = 64$. In order to ensure a stable dynamic angle, the physical time simulated was 6 s. This time was sufficient to produce a steady slope profile during the rotation. The angle was determined from the last iteration of the simulations. In the Fig. 14, the start and the end of a simulation of the dynamic angle of repose is shown. In this figure, a final angle of repose of 34.6° was obtained.

Fig. 13 shows the influence of the intergranular friction coefficients on the angle of repose. As expected, the higher the friction coefficients, the higher the angles of repose. In general, the sliding friction coefficient has a larger influence on the angle of repose, and the rolling friction coefficient is more relevant when the sliding friction coefficient is large.

The experimental results of the area method with the surface covered with granules are shown in Fig. 15. The simulations were performed as the previous one, with 200000 granules and a scale factor of $\lambda = 64$. The results indicate a little variation of the area for a wide range of rotational speeds (from 4 to 80 rpm). Nevertheless, when the rotational speed overcomes 100 rpm (105 and 116 rpm) the differences of the occupied area depending on the rotational speed become evident.

Fig. 16 shows the evolution of the CSA occupied by the powder, depending on the rotational speed and the intergranular friction coefficients used. These coefficients correspond to the pairs ($\mu_{s,g-g}$, $\mu_{r,g-g}$) obtained by simulation that reproduce the dynamic angle of repose: ($\mu_{\mathrm{r}} = 0.2$, $\mu_{\mathrm{s}} = 0.8$), ($\mu_{\mathrm{r}} = 0.3$, $\mu_{\mathrm{s}} = 0.33$), ($\mu_{\mathrm{r}} = 0.5$, $\mu_{\mathrm{s}} = 0.27$), where $\mu_{\mathrm{r}} = \mu_{\mathrm{r,g-g}} = \mu_{\mathrm{r,g-s}}$ and $\mu_{\mathrm{s}} = \mu_{\mathrm{s,g-g}} = \mu_{\mathrm{s,g-s}}$. The physical time simulated was 6 seconds for the rotation speeds of 4, 40 and 80 rpm, and 3 seconds for the cases at 105 and 116 rpm. All CSAs were obtained from the last iteration of the calculation, with the same procedure already used experimentally. In the last iteration of the calculation, all CSAs were stable except for the pair ($\mu_{\mathrm{r}} = 0.5$ and $\mu_{\mathrm{s}} = 0.27$) at the maximum rotational speed, where the steady state was not reached (hence, it was not considered).

At low rotational speeds (between 4 and 80 rpm), all simulations agree very well with the experimental case. However, at high rotational speeds (105 and 116 rpm), the pair ($\mu_{\mathrm{r}} = 0.2$, $\mu_{\mathrm{s}} = 0.8$) is the only one that can capture satisfactorily the experimental case. With this pair of values, the maximum error in all cases is less than 10 %. As a consequence, the pair ($\mu_{\mathrm{r}} = 0.2$, $\mu_{\mathrm{s}} = 0.8$) was selected as the best pair of intergranular coefficients which simultaneously reproduce the dynamic angle of repose and the evolution of the CSA occupied by the powder in the rotating drum.

4.3. *Determination of the granule-boundary friction coefficients*

The same procedure used to obtain $\mu_{s,g-g}$ and $\mu_{r,g-g}$ was performed to determine the pair of ($\mu_{s,g-s}$, $\mu_{r,g-s}$) for each type of surface considered. Once the intergranular friction coefficients were known, several simulations of the dynamic angle of repose and the area method were carried out like in the previous case. The experimental angles of repose obtained with different surfaces are collected in Table 2.

Because of the similarity of the experimental results for the surface of spray-dried powder and aluminium, the same pairs of values reproducing the dynamic angle of repose were assigned to both. Besides, due to the similarity between the results of the PP and PTFE surfaces, both are considered equal.

Fig. 17 presents the values of the dynamic angle of repose varying the sliding and rolling friction coefficients for the granule-boundary contact, using the intergranular friction coefficients previously determined. The rest of simulation parameters were the same as before. The mean experimental dynamic angle of repose for the polymeric surfaces is represented using a dashed line. As it can be observed, the variation of the dynamic angle of repose with this friction coefficients is small. For example, when $\mu_{r,g-s} = 0.001$, the maximum error in the reproduction of the experimental angle of repose with $\mu_{s,g-s} \in [0.2,...,0.7]$ is less than 1°. However, for the same range of $\mu_{s,g-s}$, if $\mu_{r,g-s} = 0.01$ the maximum error is approximately 2°.

The error generated in the reproduction of the experimental dynamic angle of repose varying $\mu_{s,g-s}$ is practically negligible if $\mu_{r,g-s} < 0.0001$. As a matter of fact, when $\mu_{r,g-s} = 0.0001$, the resulting angle of repose remains constant if $\mu_{s,g-s} < 0.7$. Only a little variation of the angle is observed when $\mu_{s,g-s} > 0.7$. This response suggests that a quite robust value has been achieved by the simulation. On the other hand, a value of $\mu_{s,g-s} < 0.18$ produced a clear slipping motion [40].

Given the small variation of the dynamic angle of repose with $\mu_{r,g-s}$ and $\mu_{s,g-s}$, pairs of ($\mu_{r,g-s}$, $\mu_{s,g-s}$) reproducing the angle of repose with an error of $\pm 0.5°$ (green band in Fig. 17) were considered suitable for the simulation of the area method.

The experimental results of the area method with different surfaces are shown in Fig. 18. Similar to section 4.2, these results present again a little variation of the area for a wide range of rotational speeds (from 4 to 80 rpm). Nevertheless, when the rotational speed exceeds 100 rpm (105 and 116 rpm), the differences between the CSA occupied by the powder are noticeable. On the one hand, the difference between using an internal coating of spray-dried powder and aluminium is negligible for all rotational speeds tested. Therefore, the same friction coefficients calibrated previously can be used as friction coefficients for the granule-aluminium contact.

On the other hand, the differences between using PP or PTFE are also very little. The maximum difference is 10 % for a rotational speed of 116 rpm. For the sake of simplicity, the differences were not considered relevant, and the same friction coefficients were assigned for both granule-PTFE and granule-PP contact. Consequently, only the friction coefficients for the polymeric surfaces needs to be determined.

To perform the simulation of the area method in this case the following pairs were selected:

($\mu_{\mathrm{r,g-s}} = 0.01$, $\mu_{\mathrm{s,g-s}} = 0.2$), ($\mu_{\mathrm{r,g-s}} = 0.001$, $\mu_{\mathrm{s,g-s}} = 0.5$), ($\mu_{\mathrm{r,g-s}} = 0.0001$, $\mu_{\mathrm{s,g-s}} = 0.7$) and ($\mu_{\mathrm{r,g-s}} = 0.0001$, $\mu_{\mathrm{s,g-s}} = 0.9$). The rest of parameters were identical to those used in section 4.2.

Fig. 19 shows the evolution of the CSA occupied by the powder, as a function of the rotational speed and the friction coefficients of the granule-boundary contact used. The experimental values depicted in Fig. 19 correspond to the mean value obtained from the two polymeric surfaces. As it can be observed, although the friction coefficients are very different from each other, the CSA occupied by the powder is practically constant for all pairs of values up to the rotational speed of 80 rpm. For rotational speeds higher than 80 rpm, the pair ($\mu_{\mathrm{r,g-s}} = 0.0001$, $\mu_{\mathrm{s,g-s}} = 0.9$) is the one that best reproduces the experimental case, particularly at high rotational speeds. The maximum error generated with this pair of values is 10 % and only when the rotational speed is 40 rpm. Notice that the other pairs of values tested do not exhibit a better behaviour at this rotational speed either, and worsen considerably at high speeds.

In summary, $\mu_{\mathrm{s,g-s}}$ should be increased to be able to reproduce correctly the area method, however, the $\mu_{\mathrm{r,g-s}}$ should be decreased to reproduce the dynamic angle of repose (Figs. 17 and 19). As a result, the pair ($\mu_{\mathrm{r,g-s}} = 0.0001$, $\mu_{\mathrm{s,g-s}} = 0.9$) represents the final calibrated values yielding the best results.

4.4 . Discussion of results

Table 3 shows the calibrated values of the granule stiffness and the sliding and rolling friction coefficients for the intergranular and granule-boundary contacts. It should be noticed that the stiffnesses for the granule-boundary contact is twice the stiffnesses for the granule-granule. This is because the surfaces are always considered elements infinitely rigid, and the contact stiffness is derived assuming two elastic springs connected in series.

On the other hand, the granule-polymer contact involves a drastic reduction of $\mu_{\mathrm{r,g-s}}$, while the effect on $\mu_{\mathrm{s,g-s}}$ is, in comparison, negligible. However, as it can be deduced from Figs. 13-19, $\mu_{\mathrm{s,g-g}}$ and $\mu_{\mathrm{r,g-g}}$ seem to have a higher impact in the model than $\mu_{\mathrm{s,g-s}}$ and $\mu_{\mathrm{r,g-s}}$.

Finally, the scaling independence study was repeated for the calibrated model, demonstrating the validity of the proposed scaling (Appendix B).

5. Conclusion

This paper proposes a straightforward methodology to obtain the main parameters of a DEM simulation based on the LSD contact law: the granule stiffnesses and the sliding and rolling friction coefficients of the intergranular and granule-boundary contacts. Currently, DEM simulations cannot handle the real number of particles present in many industrial processes. Therefore, with the aim of making this approach feasible for industrial applications, this paper also proposes a set of scaling laws where the size and the stiffnesses of the granules are conveniently modified. This procedure makes it possible to keep unaltered the dynamic response of the simulated spray-dried powder when the collisional regime dominates over the external confining pressures. This approach demonstrates that only one experimental setup was required to calibrate the powder model: a rotating drum.

To calibrate a spray-dried powder for industrial-oriented purposes, four assumptions have been adopted:

(i) the stiffness of all particles in the system is considered equal.
(ii) the damping coefficient is the 70 % of critical damping coefficient assuming quasi-static conditions (no rate-dependency of the restitution coefficient).
(iii) a covered surface of granules is approximately equal to a surface with granular properties.
(iv) the influence of the end plates of the rotating drum is negligible in the powder dynamics compared to the inner surface effect.

This proposal enables the characterization of different types of powders independently of their GSD, just by using a single experimental setup. In this sense, this work not only presents the calibration procedure but also its applicability by testing four types of material surfaces in contact with the powder.

The main advantages of the proposed methodology over others (such as methods based on shear cell tests) to calibrate DEM models are the simplicity of the tests and the short simulation times involved. Furthermore, the presented procedure to calibrate the friction coefficients does not involve external loads, as the shear cell tests do. This is an advantage if the real stiffnesses cannot be used in the simulations as with the tested spray-dried powder, whose real stiffness involves too small time steps to perform feasible simulations. Additionally, the presented procedure is specially suitable to calibrate powder models to be used for simulating highly dynamic processes. This is because the area method presented makes it possible to characterize the powder in a dynamic regime, which can also be adjusted depending on the final application of the model.

Regarding the limitations, the proposed methodology uses a manual image treatment, which involves an inherent error in the measurements depending on the researcher who performs it. It produces, inevitably, less accurate results than the one obtained using a ring shear test, for example. In the future, a way to automate the measurement of the dynamic angle of repose and the image analysis should be investigated. Additionally, other calibration test could be investigated, such as the use of a FT4 rheometer. The authors encourage readers to assess more accurate tests to determine the friction coefficients, but meeting the requirements of easiness and quickness (highly demanded by industrial environments). Furthermore, the proposed methodology does not provide a calibration test for viscous damping, which is fixed at its theoretical value in quasi-static conditions. A customized test should be addressed to properly calibrate this parameter before the calibration of the friction coefficients.

Finally, it is worth mentioning that the proposed scaling laws as well as the simulation strategy are also valid for simulating any powder-based process, independently of their size. Therefore, it has an immediate applicability in the modelling of large granular flows and in the design of powder equipment.

6. Acknowledgements

The authors of this paper wish to thank MACER S.L and the CDTI Ministry of Science and Innovation of Spain, as part of the project with the reference number: IDI20140989. Specially, J.M. Tiscar wishes to thank the Conselleria de Educació i Ciència de la Generalitat Valenciana for its financial support in the conducted study with a PhD scholarship, through the programme VALi+D for researchers training. The authors deeply thank the reviewers for their thoughtful and valuable comments towards improving this manuscript.

Appendix A. Computational verification of the DEM framework

DEM simulations performed in this paper have been done using an in-house DEM framework entirely developed by the authors. Despite a forthcoming publication will deal extensively with the development of this in-house framework, for the sake of completeness a computational verification of the model and a benchmark are described below.

Appendix A.1. Model verification

The purposed model detailed in section 2 was included in a DEM framework developed using the C++ programming language. To verify the model implementation, a simple test was executed and compared with the same model implemented in Scilab.

The verification test consisted in dropping two vertically aligned particles on a flat surface. A schematic of the test is depicted in Fig. A.1, where R_1 and R_2 are the radii of the particles 1 and 2, respectively, $\mathbf{r}_1$ and $\mathbf{r}_2$ are the positions, ρ_1 and ρ_2 are the densities, and ω_1 is the initial angular velocity of the particle 1. Initial conditions and the model parameters used in the verification test are depicted in Table A.1.

Fig. A.2 shows the trajectories of both particles after 5 seconds of simulation. The results of the DEM framework match with those obtained from Scilab, validating the computational implementation of the equations of the model. The Scilab script used in this section can be consulted in the Supplementary Material attached to this paper.

Appendix A.2. Benchmarking

DEM framework implementation was verified by comparing it with one of the most widely used software packages for DEM simulations, LIGGGHTS [51]. The verification was made comparing the number of contacts and the total kinetic energy of the particles involved during a silo discharge.

The discharge of the silo consisted in dropping the particles from the silo in a vessel (Fig. A.3). It is also worth emphasizing that LIGGGHTS does not include exactly the same contact model used in this paper. In order to perform a fairy comparison and use the same contact model in both implementations, some model parameters such as damping coefficient and rolling friction were set to 0 (note that LIGGGHTS considers the tangential damping coefficient, which was also set to 0). Table A.2 includes all model parameters used in the simulation of the silo discharge.

Fig. A.4 presents the evolution of the number of contacts in both implementations. At the beginning of the discharge, the number of contacts decreases during the first 12 seconds. From this point on, the number of contacts increases until the total discharge occurs, reaching a constant value. As it can be appreciated, both implementations give essentially the same results.

On the other hand, Fig. A.5 shows the evolution of the total kinetic energy of the particles during the silo discharge. When the discharge begins, the total kinetic energy increases rapidly, and it gradually reduces as the discharge progresses. The differences between both implementations are small, which are attributable to the different integration schemes used (LIGGGHTS uses the velocity Verlet scheme, while the DEM framework developed uses the basic Verlet scheme).

Appendix B. Scaling independence study

DEM simulations performed in this paper required a granule upscaling to be computationally feasible to simulate realistic industrial processes. Although several granule properties were corrected to keep constant the macroscopic response of the powder bulk, it is essential to ensure that the solution is not affected by the scaling applied. After calibrating the model, the scaling independence study was repeated for each experiment, in order to increase the confidence in the calibrated values and the scaling applied.

Fig. B.1 shows the scaling effect of the calibrated model in the confined Young's modulus, obtained following the procedure described in section 3.2.1. No relevant differences in the confined Young's modulus was noticed between the scale factors tested. On the other hand, it is worth mentioning that a greater reduction of the scale factor was not carried out because it was not computationally feasible due to the computation time required (in the order of months) with the computer resources available.

Fig. B.2 illustrates the scaling effect of the calibrated model in the coordination number (section 4.1). For λ values ranging from 8 to 125, the variation of the coordination number was found very small (notice that with the calibrated friction coefficients, the resulting coordination number is lower than expected according to the Fig. 12). This proves that, for the values of λ tested, the structure of the scaled powder bulk represents very well the unscaled one.

The scaling effect of the calibrated model in the dynamic angle of respose and in the CSA of the drum occupied by the powder are shown in Table B.1. In all cases, the inner surface of the drum is considered to be aluminium. Regarding the dynamic angle of response, a difference of 1° is observed between a model where the diameter of the granules is scaled twice and another one in which it is scaled four times, although the granule distribution pattern remains the same (Fig. B.3). The influence of the scale factor in the dynamic angle of repose may be related to the nature of the measure, which depends on the size of the powder [40]. Nevertheless, according to the Table B.1, the difference of the dynamic angle of repose between the unscaled model and the scaled one with the scale factor selected in sections 4.2 and 4.3 ($\lambda = 64$) is expected to be about 1°.

Regarding the CSA of the drum occupied by the powder, notice that it is not clearly independent of the scale factor. Similar to the case of the dynamic angle of repose, this behaviour may be related to the influence of the size of the powder in the measure. Anyhow, despite this slight impact of the scaling, the differences between the unscaled model and the scaled one with the scale factor used in the CSA measurement ($\lambda = 64$) is less than 4 %.

References

[1] J. S. Reed, Principles of ceramics processing, Wiley New York, 2 edition, 1995.

703 [2]J. S. Reed, From batch to pressed tile: mechanics and system microstructural changes, in: QUALICER 6th World Congress on 704 Ceramic Tile Quality, Spain, p. 20.

[3] R. Galindo, Prensas, moldes y prensado en la fabricación de baldosas cerámicas [Presses, molds and pressing in the manufacture of ceramic tiles], MACER, 2008.

[4] J. L. Amorós, J. E. Enrique, A. Escardino, et al., Defectos de fabricación de pavimentos y revestimientos cerámicos [Manufacturing defects of wall and floor tiles], AICE-ITC, 1991.

[5] P. A. Cundall, O. D. L. Strack, A discrete numerical model for granular assemblies, Géotechnique 29 (1979) 47–65.

[6] S. Luding, Collisions & Contacts between two particles, Physics of dry granular media - NATO ASI Series E350 1 (1998) 285.

[7] S. Luding, Cohesive, frictional powders: Contact models for tension, Granular Matter 10 (2008) 235–246.

[8] M. Sakai, S. Koshizuka, Large-scale discrete element modeling in pneumatic conveying, Chemical Engineering Science 64 (2009) 533–539.

[9] C. J. Coetzee, D. N. J. Els, Calibration of discrete element parameters and the modelling of silo discharge and bucket filling, Computers and Electronics in Agriculture 65 (2009) 198–212.

[10] Z. Zhang, L. Liu, Y. Yuan, A. Yu, A simulation study of the effects of dynamic variables on the packing of spheres, Powder Technology 116 (2001) 23–32.

[11] C. Bierwisch, T. Kraft, H. Riedel, M. Moseler, Die filling optimization using three-dimensional discrete element modeling, Powder Technology 196 (2009) 169–179.

[12] M. Rahman, K. Shinohara, H. Zhu, A. Yu, P. Zulli, Size segregation mechanism of binary particle mixture in forming a conical pile, Chemical Engineering Science 66 (2011) 6089 – 6098.

[13] K. Odagi, T. Tanaka, K. Yamane, Rough-Surface and Its Application to DEM Simulation of Compression Test of Particles, in: Discrete Element Methods: Numerical Modeling of Discontinua, ASCE, 2002, pp. 299–304.

[14] V. Buchholtz, T. Pöschel, H.-J. Tillemans, Simulation of rotating drum experiments using non-circular particles, Physica A 216 (1995).

[15] Y. Guo, C.-Y. Wu, K. Kafui, C. Thornton, 3D DEM/CFD analysis of size-induced segregation during die filling, Powder Technology 206 (2011) 177–188.

[16] Y. Tsunazawa, Y. Shigeto, C. Tokoro, M. Sakai, Numerical simulation of industrial die filling using the discrete element method, Chemical Engineering Science 138 (2015) 791–809.

[17] A. P. Grima, Quantifying and modelling mechanisms of flow in cohesionless and cohesive granular materials, Ph.D. thesis, University of Wollongong, 2011.

[18] C. J. Coetzee, E. Horn, Calibration of the Discrete Element Method Using a Large Shear Box, International Journal of Mechanical, Aerospace, Industrial, Mechatronic and Manufacturing Engineering 8 (2014) 2105–2114.

[19] T. Roessler, C. Richter, A. Katterfeld, F. Will, Development of a standard calibration procedure for the dem parameters of cohesionless bulk materials – part i: Solving the problem of ambiguous parameter combinations, Powder Technology 343 (2019) 803 – 812.

[20] H. Cheng, T. Shuku, K. Thoeni, H. Yamamoto, Probabilistic calibration of discrete element simulations using the sequential quasi-monte carlo filter, Granular Matter 20 (2018) 11.

[21] P. S. Desai, A. Mehta, P. S. Dougherty, C. F. Higgs, A rheometry based calibration of a first-order dem model to generate virtual avatars of metal additive manufacturing (am) powders, Powder Technology 342 (2019) 441 – 456.

[22] C. Coetzee, Review: Calibration of the discrete element method, Powder Technology 310 (2017) 104 – 142.

[23] A. P. Grima, P. W. Wypych, Development and validation of calibration methods for discrete element modelling, Granular Matter 13 (2010) 127–132.

[24] E. Horn, The Calibration of Material Properties for Use in Discrete Element Models by, Ph.D. thesis, University of Stellenbosch, 2012.

[25] C. Thornton, L. Zhang, Numerical Simulations of the Direct Shear Test, Chemical Engineering & Technology 26 (2003) 153–156.

[26] C. O'Sullivan, L. Cui, J. D. Bray, Three-dimensional discrete element simulations of direct shear tests, in: 2nd International PFC Symposium, A.A. Balkema Publishers, 2004, p. 10.

[27] J. Härtl, J. Y. Ooi, Numerical investigation of particle shape and particle friction on limiting bulk friction in direct shear tests and comparison with experiments, Powder Technology 212 (2011) 231 – 239.

[28] L. Cui, C. O'Sullivan, Exploring the macro-and micro-scale response of an idealised granular material in the direct shear apparatus, Geotechnique 56 (2006) 455–468.

[29] A. Di Renzo, F. P. Di Maio, Comparison of contact-force models for the simulation of collisions in DEM-based granular flow codes, Chemical Engineering Science 59 (2004) 525–541.

[30] C. Thornton, S. J. Cummins, P. W. Cleary, An investigation of the comparative behaviour of alternative contact force models during elastic collisions, Powder Technology 210 (2011) 189 – 197.

[31] D. A. Santos, M. A. Barrozo, C. R. Duarte, F. Weigler, J. Mellmann, Investigation of particle dynamics in a rotary drum by means of experiments and numerical simulations using dem, Advanced Powder Technology 27 (2016) 692 – 703.

[32] F. A. Gilabert, J.-N. Roux, A. Castellanos, Computer simulation of model cohesive powders: Plastic consolidation, structural changes, and elasticity under isotropic loads, Phys. Rev. E 78 (2008) 031305.

[33] S. C. Thakur, H. Ahmadian, J. Sun, J. Y. Ooi, An experimental and numerical study of packing, compression, and caking behaviour of detergent powders, Particuology 12 (2014) 2 – 12. Special issue on conveying and handling of particulate solids – Challenges of discrete element simulation, application and calibration.

[34] F. Ercolessi, A molecular dynamics primer, Spring college in computational physics, ICTP, Trieste 19 (1997).

[35] I. C. Group, PFC2D 2.00 Particle Flow Code in Two Dimensions, 1998.

[36] J. E. Hilton, P. W. Cleary, Comparison of non-cohesive resolved and coarse grain DEM models for gas flow through particle beds, Applied Mathematical Modelling 38 (2014) 4197–4214.

[37] S. Lommen, M. Mohajeri, G. Lodewijks, D. Schott, Dem particle upscaling for large-scale bulk handling equipment and material interaction, Powder Technology 352 (2019) 273 – 282.

[38] T. Roessler, A. Katterfeld, Scaling of the angle of repose test and its influence on the calibration of dem parameters using upscaled particles, Powder Technology 330 (2018) 58 – 66.

[39] C. Coetzee, Particle upscaling: Calibration and validation of the discrete element method, Powder Technology 344 (2019) 487 – 503.

[40] J. Mellmann, The transverse motion of solids in rotating cylinders–forms of motion and transition behavior, Powder Technology 118 (2001) 251–270.

[41] A. Santomaso, Y. Ding, J. Lickiss, D. York, Investigation of the Granular Behaviour in a Rotating Drum Operated over a Wide Range of Rotational Speed, Chemical Engineering Research and Design 81 (2003) 936–945.

[42] C. A. Schneider, W. S. Rasband, K. W. Eliceiri, NIH Image to ImageJ: 25 years of image analysis, Nature methods 9 (2012) 671.

[43] A. de Ryck, H. Zhu, S. Wu, A. Yu, P. Zulli, Numerical and theoretical investigation of the surface flows of granular materials on heaps, Powder Technology 203 (2010) 125 – 132.

[44] G. Lumay, F. Boschini, K. Traina, S. Bontempi, J.-C. Remy, R. Cloots, N. Vandewalle, Measuring the flowing properties of powders and grains, Powder Technology 224 (2012) 19 – 27.

[45] D. Geldart, E. Abdullah, A. Verlinden, Characterisation of dry powders, Powder Technology 190 (2009) 70 – 74. Selection of Papers from the Symposium Powder Science and Technology - Powders and Sintered Material STP-PMF 2007.

[46] C. M. Dury, G. H. Ristow, J. L. Moss, M. Nakagawa, Boundary effects on the angle of repose in rotating cylinders, Physical Review E 57 (1998) 4491.

[47] M. W. Johnstone, Calibration of DEM models for granular materials using bulk physical tests, Ph.D. thesis, University of Edinburgh, 2010.

[48] S. Lommen, D. Schott, G. Lodewijks, DEM speedup: Stiffness effects on behavior of bulk material, Particuology 12 (2014) 107–112.

[49] H. Kuo, P. Knight, D. Parker, Y. Tsuji, M. Adams, J. Seville, The influence of DEM simulation parameters on the particle behaviour in a V-mixer, Chemical Engineering Science 57 (2002) 3621–3638.

[50] M. Paulick, M. Morgeneyer, A. Kwade, Review on the influence of elastic particle properties on DEM simulation results, Powder Technology 283 (2015) 66–76.

[51] CFDEM® Project, LIGGGHTS – Open-Source Discrete Element Simulations of Granular Materials Based on LAMMPS. Documentation. Versión 3.X, https://www.cfdem.com/media/DEM/docu/Manual.html (Acceso: 2018-03-07), 2018.

[52] D. Ladipo, V. Puri, Computer controlled shear cell for measurement of flow properties of particulate materials, Powder Technology 92 (1997) 135–146.

[53] I. Opalinski, M. Chutkowski, M. Stasiak, Characterizing moist food-powder flowability using a Jenike shear-tester, Journal of Food Engineering 108 (2012) 51–58.

[54] R. Bharadwaj, W. R. Ketterhagen, B. C. Hancock, Discrete element simulation study of a Freeman powder rheometer, Chemical Engineering Science 65 (2010) 5747–5756.

[55] S. K. Wilkinson, S. A. Turnbull, Z. Yan, E. H. Stitt, M. Marigo, A parametric evaluation of powder flowability using a Freeman rheometer through statistical and sensitivity analysis: A discrete element method (DEM) study, Computers & Chemical Engineering 97 (2017) 161–174.

Tables

Table 1. Elapsed time for the typical tests performed to calibrate DEM parameters.

Test	Volume of powder (cm^3)	Elapsed time (s)	References
Confined compression	65	30	This paper
Jenike shear cell	50	30-100*	[52, 53]
FT4 rheometer	100	12	[54, 55]
Dynamic angle of repose	148	6	This paper

*It strongly depends on the type of powder and the normal load applied.

Table 2. Dynamic angle of repose for the spray-dried powder with different drum inner surfaces.

Surface Material	Dynamic angle of repose (°)
PTFE	31.9
PP	32.2
Aluminium	34.2
Spray-dried powder	34.6

Table 3. Calibrated parameters of the model.

Granule-Granule Contact	Granule density, ρ_g (kg/m^3)		1800
	Normal stiffness, k_n (N/m)		200
	Tangential stiffness, k_s (N/m)		200
	Rolling stiffness, k_r (N/m)		200
	Damping ratio, ξ		0.7
	Sliding friction coefficient, $\mu_{s,g-g}$		0.8
	Rolling friction coefficient, $\mu_{r,g-g}$		0.2
Granule-Boundary Contact	Normal stiffness, k_n (N/m)		400
	Tangential stiffness, k_s (N/m)		400
	Rolling stiffness, k_r (N/m)		400
	Damping ratio, ξ		0.7
	Sliding friction coefficient, $\mu_{s,g-s}$	Aluminium	0.8
		PP	0.9
		PTFE	0.9
	Rolling friction coefficient, $\mu_{r,g-s}$	Aluminium	0.2

		PP	0.0001
		PTFE	0.0001

Table A.1. Initial conditions and parameters used in the model verification.

Particle 1	Radius, R_1 (m)	0.025
	Density, ρ_1 (kg/ m^3)	500
	Position, $\mathbf{r}_1(r_{1x}, r_{1y}, r_{1z})$ (m)	(0,0.5,0)
	Linear Velocity, $\mathbf{v}_1(v_{1x}, v_{1y}, v_{1z})$ (m/s)	(0,0,0)
	Angular Velocity, $\boldsymbol{\omega}_1(\omega_{1x}, \omega_{1y}, \omega_{1z})$ (rad/s)	(0,0,-300)
Particle 2	Radius, R_2 (m)	0.03
	Density, ρ_2 (kg/ m^3)	500
	Position, $\mathbf{r}_2(r_{2x}, r_{2y}, r_{2z})$ (m)	(0,0.2,0)
	Linear Velocity, $\mathbf{v}_2(v_{2x}, v_{2y}, v_{2z})$ (m/s)	(0,0,0)
	Angular Velocity, $\boldsymbol{\omega}_2(\omega_{2x}, \omega_{2y}, \omega_{2z})$ (rad/s)	(0,0,0)
Particle 1 - Particle 2 Contact	Normal stiffness, k_n (N/m)	200
	Tangential stiffness, k_s (N/m)	200
	Rolling stiffness, k_r (N/m)	200
	Damping ratio, ξ	0.7
	Sliding friction coefficient, μ_s	0.5
	Rolling friction coefficient, μ_r	0.2
Particle 1 – Surface Contact	Normal stiffness, k_n (N/m)	400
	Tangential stiffness, k_s (N/m)	400
	Rolling stiffness, k_r (N/m)	400
	Damping ratio, ξ	0.7
	Sliding friction coefficient, μ_s	0.8
	Rolling friction coefficient, μ_r	0.2
Particle 2 – Surface Contact	Normal stiffness, k_n (N/m)	400
	Tangential stiffness, k_s (N/m)	400

	Rolling stiffness, k_r (N/m)	400
	Damping ratio, ξ	0.7
	Sliding friction coefficient, μ_s	0.8
	Rolling friction coefficient, μ_r	0.2
Simulation Conditions	Time step, Δt (s)	0.0001
	Physical time, t (s)	5

Table A.2 All parameters used in the benchmark.

Particles	Particle Size	d_{50} (m)	1.0
	Distribution (PSD)	σ_{geo}	1.1
	Density, ρ (kg/ m^3)		500
Particle – Particle Contact	Normal stiffness, k_n (N/m)		50000
	Tangential stiffness, k_s (N/m)		50000
	Rolling stiffness, k_r (N/m)		0
	Damping ratio, ξ		0.0
	Sliding friction coefficient, μ_s		0.5
	Rolling friction coefficient, μ_r		0.0
Particle – Surface Contact	Normal stiffness, k_n (N/m)		100000
	Tangential stiffness, k_s (N/m)		100000
	Rolling stiffness, k_r (N/m)		0
	Damping ratio, ξ		0.0
	Sliding friction coefficient, μ_s		0.5
	Rolling friction coefficient, μ_r		0.0
Simulation Conditions	Time step, Δt (s)		0.001
	Physical time, t (s)		120

Table B.1. Scaling effect of the calibrated model in the dynamic angle of respose and in the CSA of the drum occupied by the powder.

Scale factor λ	Dynamic angle of repose (°)	CSA (%)

8	33.4	43.9
27	33.9	44.5
64	34.6	45.5

Figures

Fig. 1. Geometrical magnitudes defining the interaction distance in the DEM.

Fig. 2. Alteration of the relative overlap between an unscaled and scaled assembly of granules according to the coarse granule model approach.

Fig. 3. Top: spray-dried powder morphology. Bottom: granule size distribution histogram.

Fig. 4. General view of the experimental setup of a confined compression test.

Fig. 5. Dynamic angle of repose test setup.

Fig. 6. Powder motion depending on the rotational speed.

Fig. 7. Execution of the image analysis to obtain the CSA of the drum occupied by the powder.

Fig. 8. Four different cylindrical surfaces. Top, left: aluminium drum. Top, right: raw drum. Bottom to top: granules, PP and PTFE.

Fig. 9. Zoomed view corresponding to the surface coated with granules.

Fig. 10. Experimental and simulated force-displacement curve from confined compression test.

Fig. 11. Confined Young's modulus calculated in the simulations, as a function of stiffness.

Fig. 12. Variation of the repose coordination number of the granules with stiffness.

Fig. 13. Effect of the intergranular friction coefficients on the dynamic angle of repose.

Fig. 14. (color online) Start and end of a simulation of the dynamic angle of repose test.

Fig. 15. CSA occupied by the powder in the drum covered with the granules surface (%).

Fig. 16. Effect of the intergranular friction coefficients on the CSA occupied by the powder (%).

Fig. 17. Effect of the granule-boundary friction coefficients on the dynamic angle of repose, with the calibrated intergranular friction coefficients.

Fig. 18. CSA occupied by the powder in the drum covered with different surfaces (%).

Fig. 19. Effect of the granule-boundary friction coefficients on the CSA occupied by the powder (%). Experimental is considered the mean value for both polymeric surfaces.

Flat Surface

Fig. A.1. Schematic of the initial condition for the model verification.

Fig. A.2. Trajectories of the two particles after 5 seconds of simulation, using the DEM framework developed and Scilab.

Fig. A.3. Left: starting of silo discharge. Right: ending of silo discharge.

Fig. A.4. Evolution of the number of contacts during the silo discharge.

Fig. A.5. Evolution of the total kinetic energy of the particles during the silo discharge.

Fig. B.1. Scaling effect in the confined Young’s modulus.

Fig. B.2. Scaling effect in the coordination number.

Fig. B.3. (color online) Scaling effect in the granule distribution pattern after completing the dynamic angle of repose test. Top: initial conditions. Bottom: final angle of repose.

Research highlights

- ► A novel methodology to calibrate DEM simulations is proposed.
- ►The methodology is focused on systems with low particle size (Φ<1mm).
- ►Scaling laws required to reduce the number of particles to simulate are shown.
- ►Spray-dried powder behaviour with several surfaces is investigated.

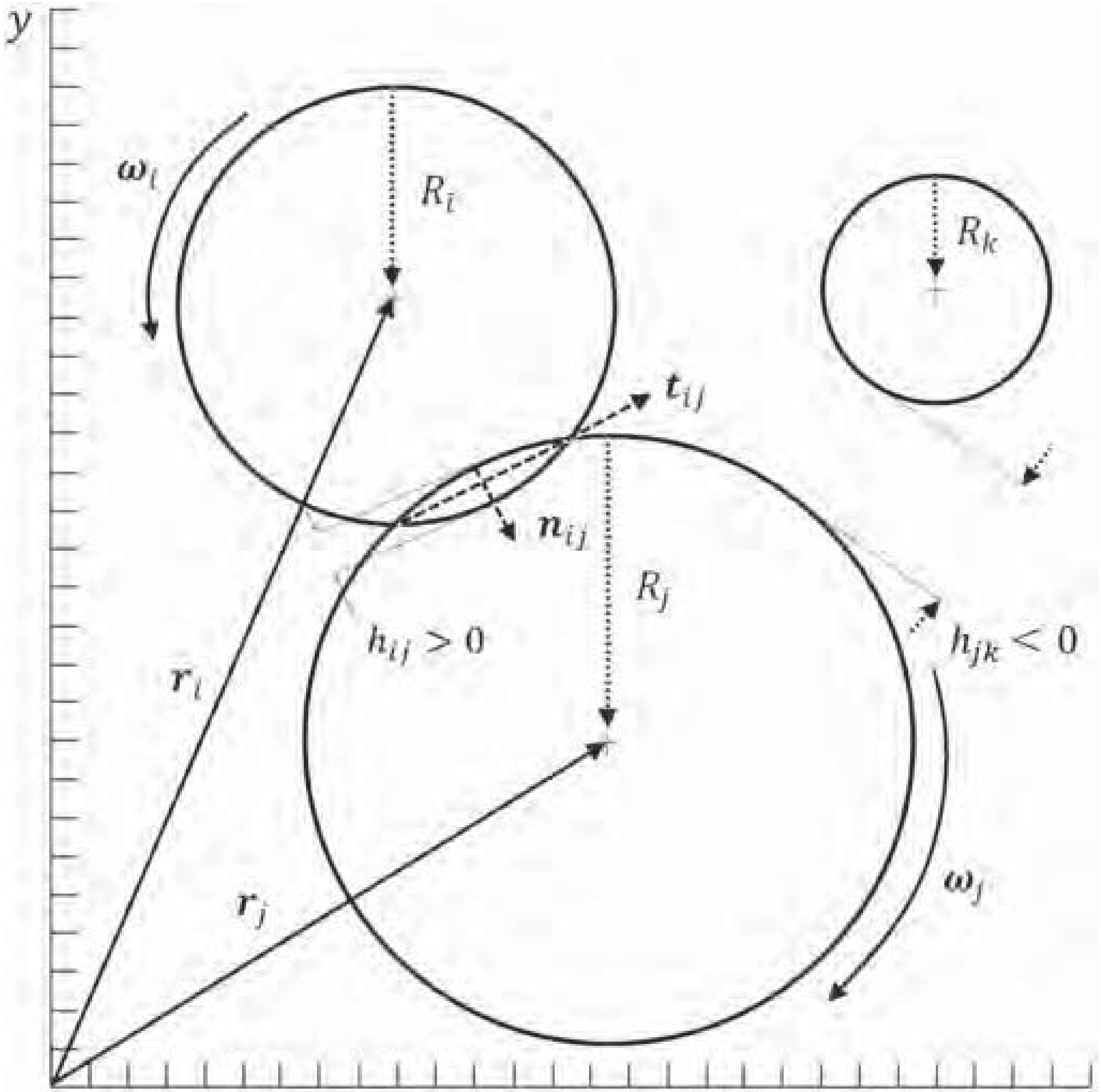

Figure 1

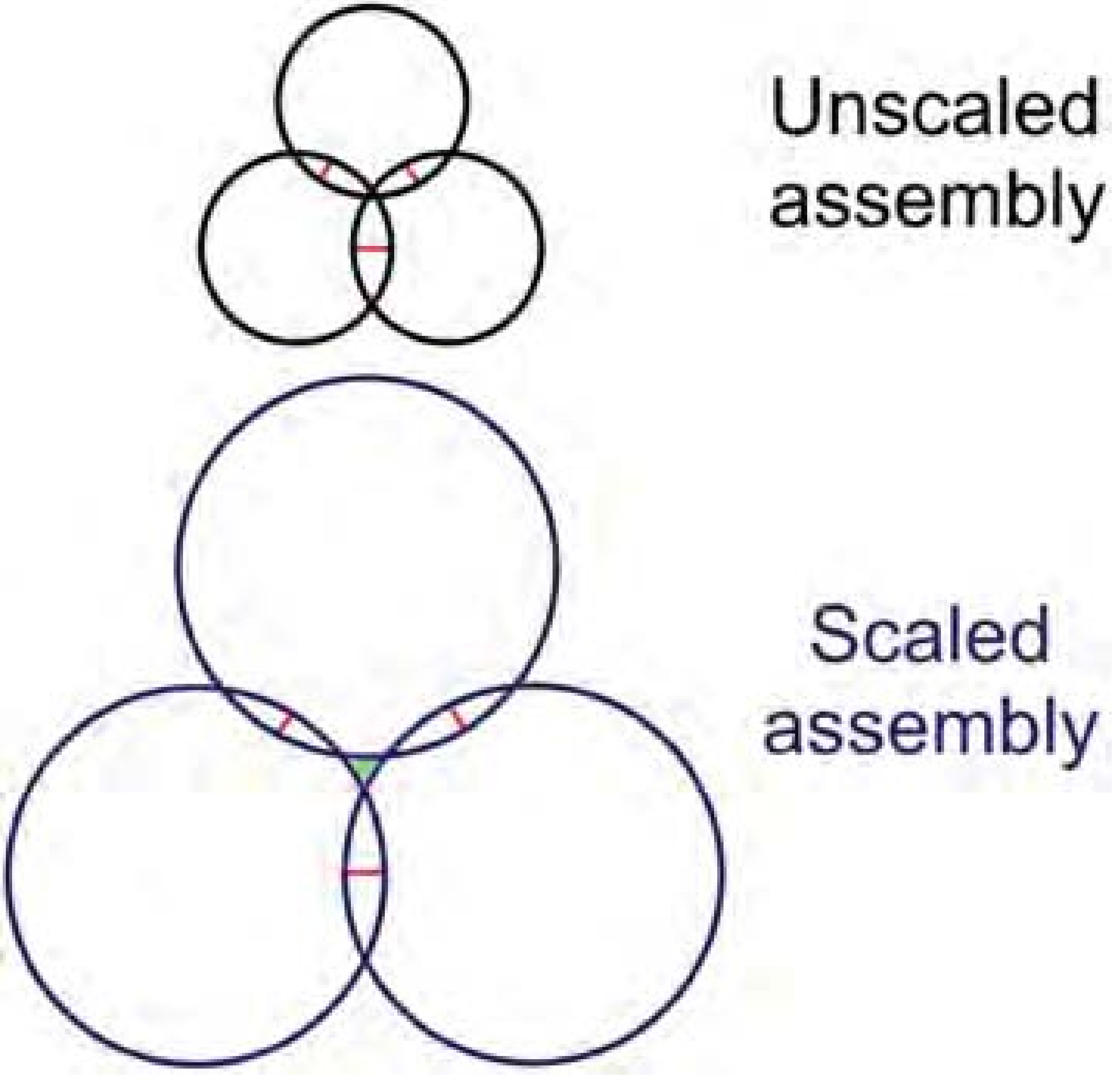

Figure 2

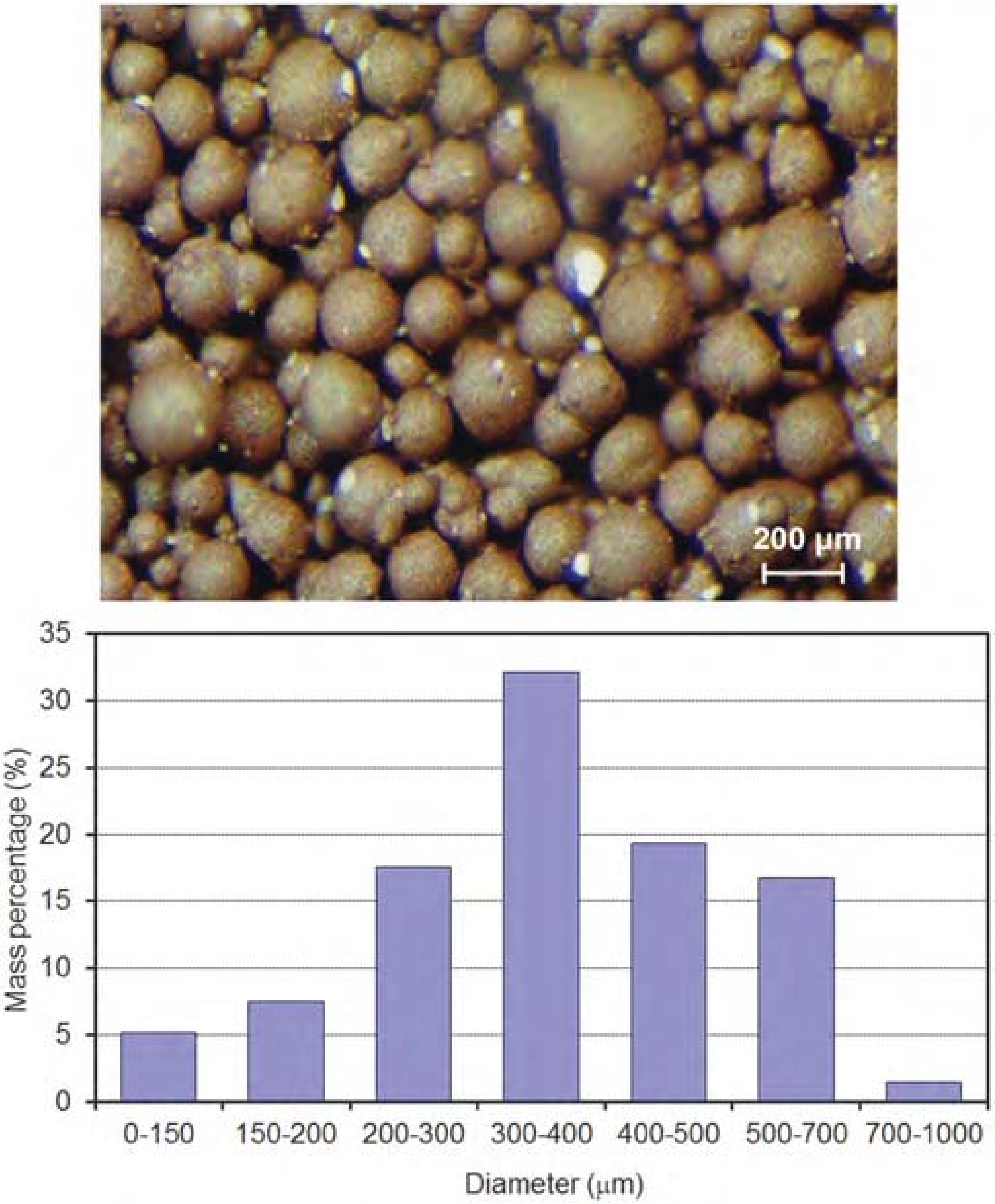
200 µm
Mass percentage (%)
0
5
10
15
20
25
30
35
0-150
150-200
200-300
300-400
400-500
500-700
700-1000
Diameter (µm)

Figure 3

Figure 4

Figure 5

(a) 4 rpm **(b)** 40 rpm **(c)** 80 rpm

(d) 105 rpm **(e)** 116 rpm

Figure 6

(a) Original image.

(b) Analyzed image.

Figure 7

Figure 8

Figure 9

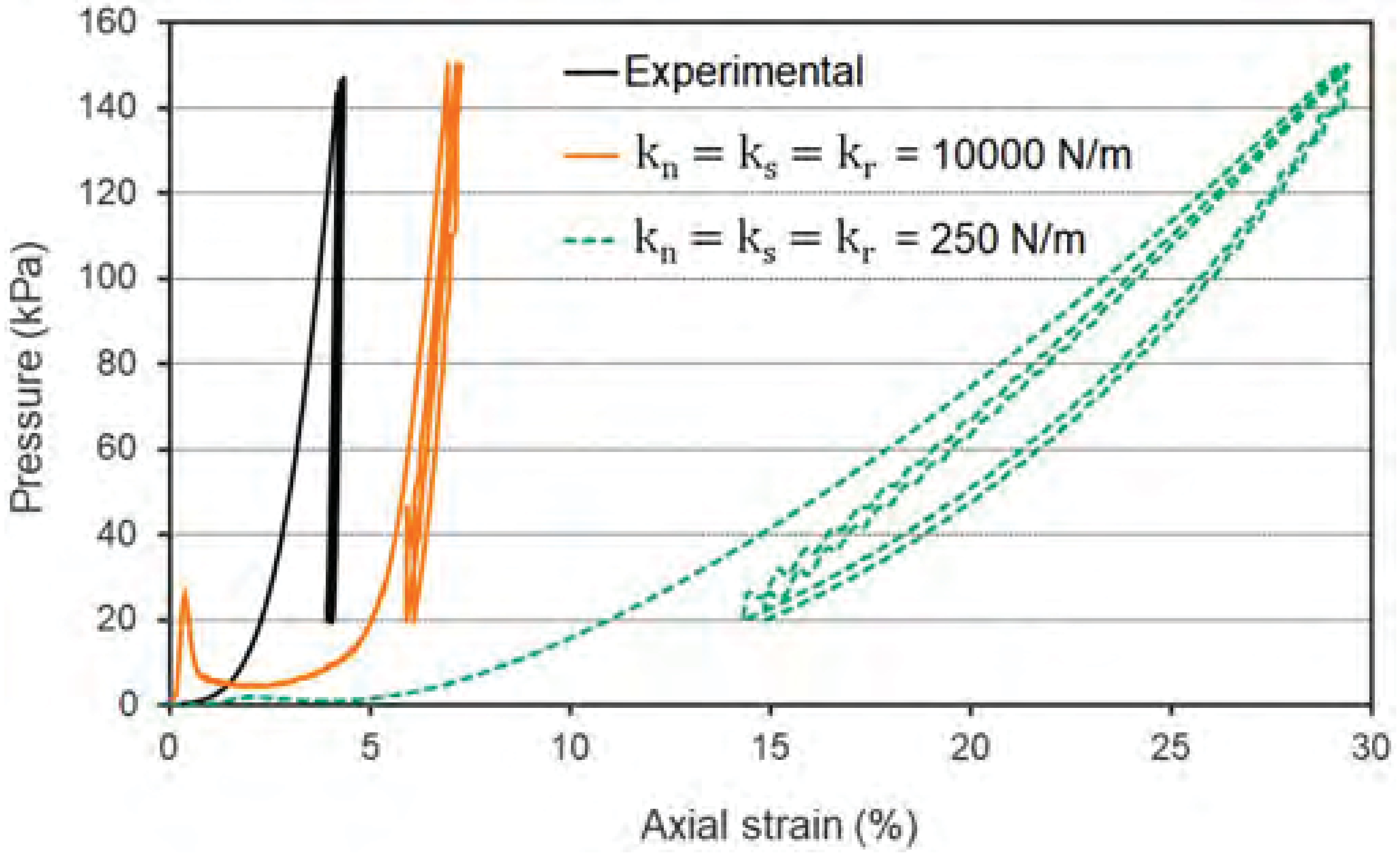
160
140
120
100
80
60
40
20
0
Pressure (kPa)
0
5
10
15
20
25
30
Axial strain (%)
Experimental
$k_n = k_s = k_r$ = 10000 N/m
$k_n = k_s = k_r$ = 250 N/m

Figure 10

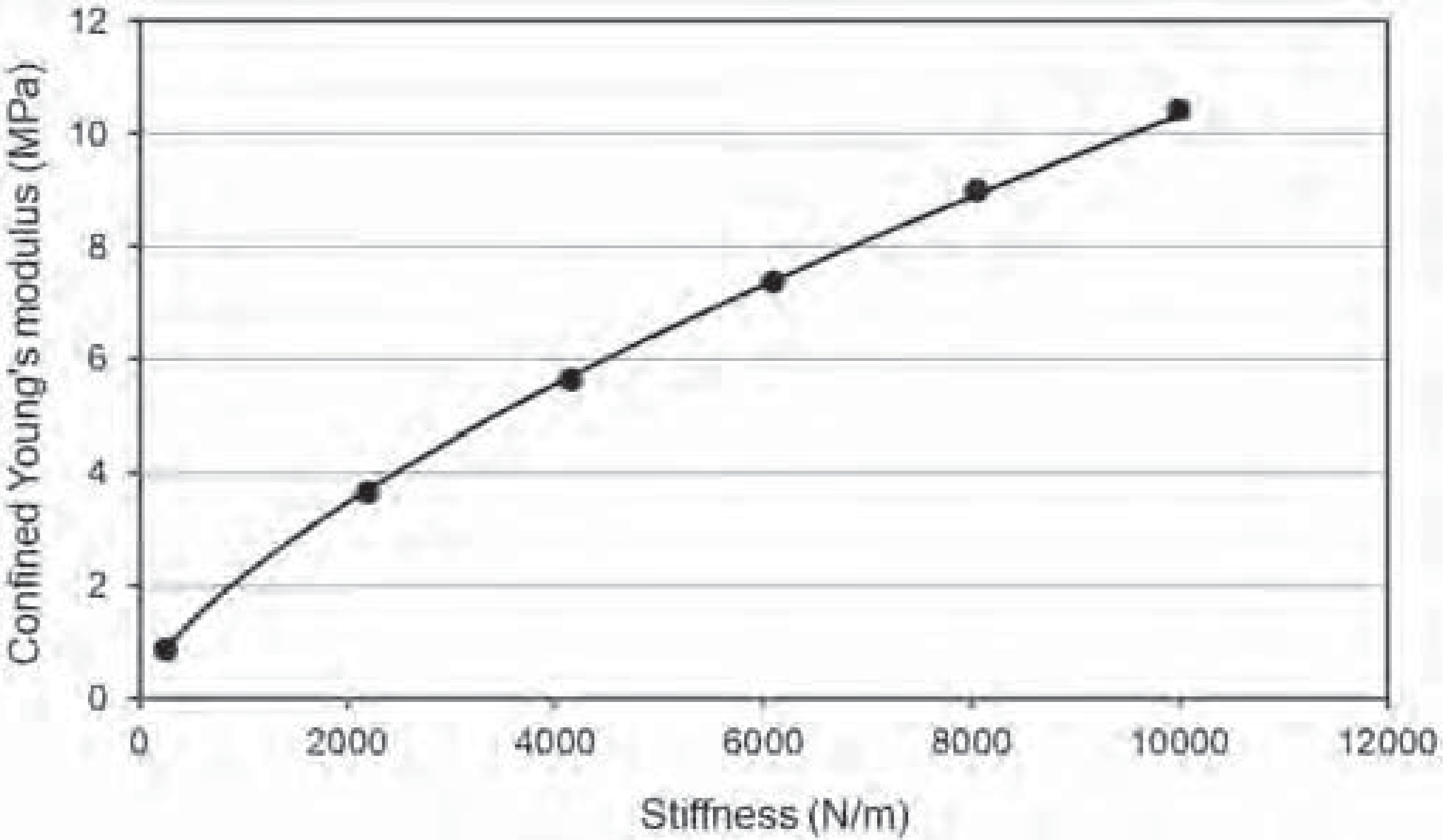
12
10
8
6
4
2
0
Confined Young's modulus (MPa)
0
2000
4000
6000
8000
10000
12000
Stiffness (N/m)

Figure 11

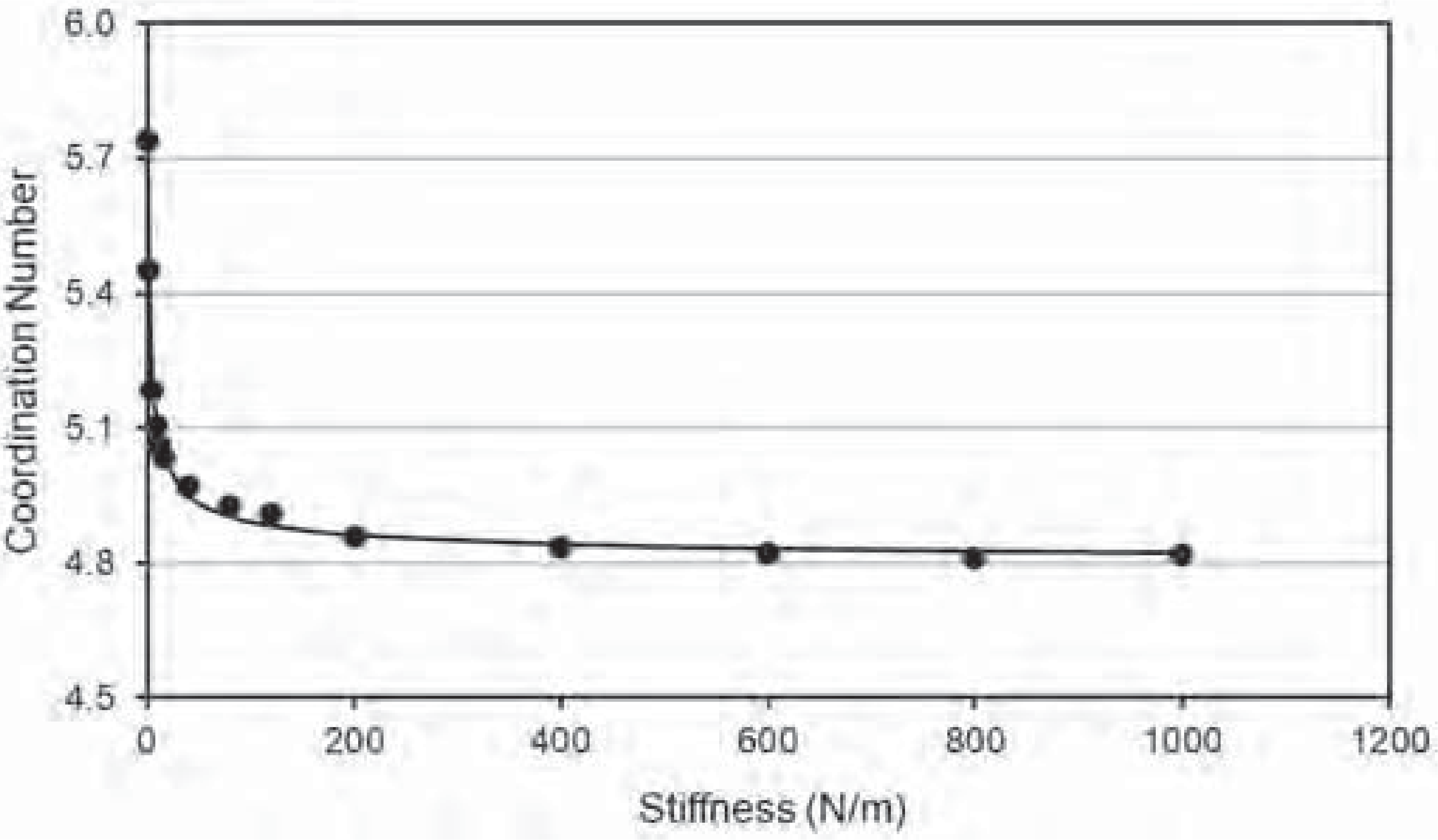
6.0
5.7
5.4
5.1
4.8
4.5
Coordination Number
0
200
400
600
800
1000
1200
Stiffness (N/m)

Figure 12

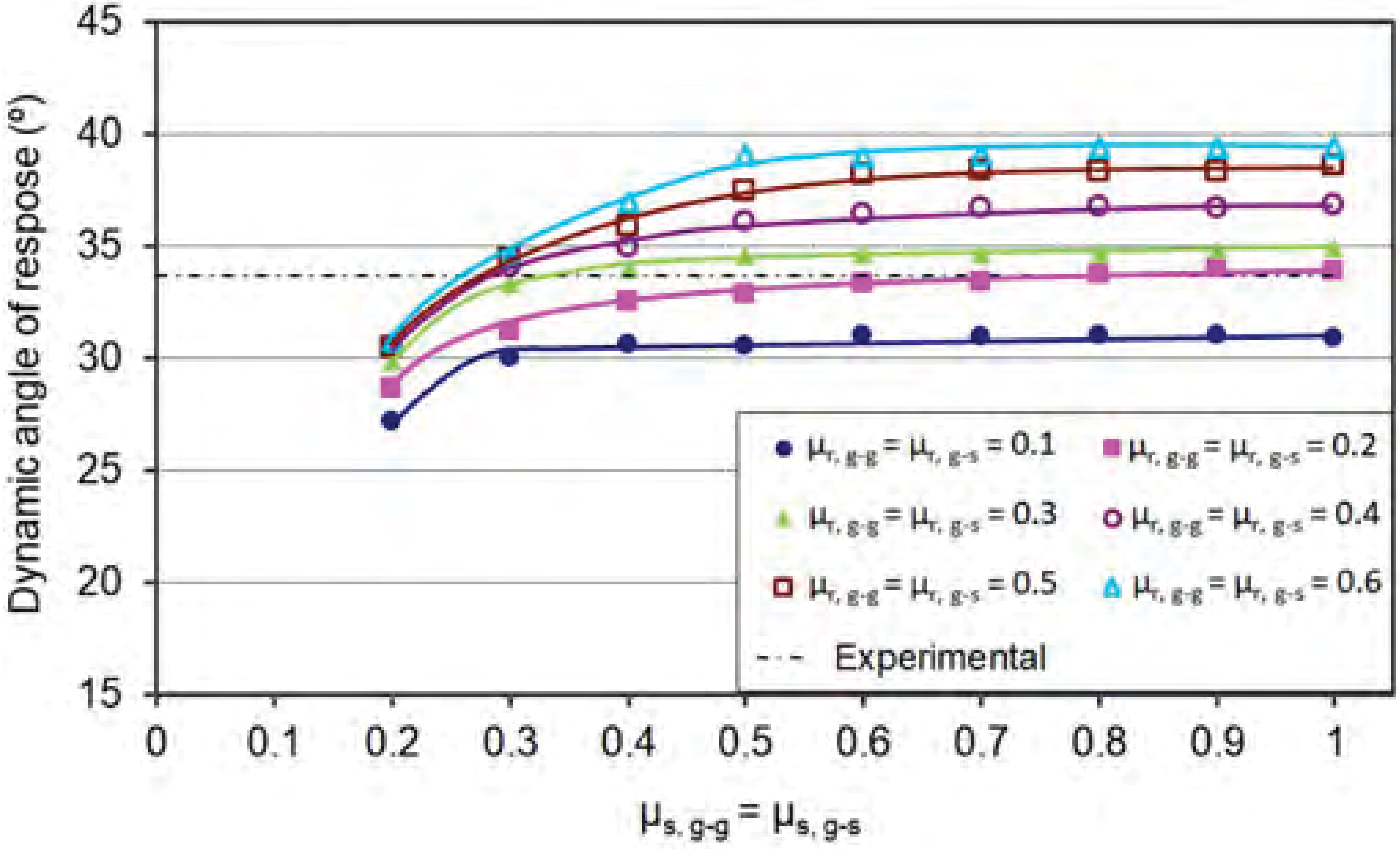
45
40
35
30
25
20
15
Dynamic angle of respose (°)
0
0.1
0.2
0.3
0.4
0.5
0.6
0.7
0.8
0.9
1
$\mu_{s,\,g\text{-}g} = \mu_{s,\,g\text{-}s}$
● $\mu_{r,\,g\text{-}g} = \mu_{r,\,g\text{-}s} = 0.1$
■ $\mu_{r,\,g\text{-}g} = \mu_{r,\,g\text{-}s} = 0.2$
▲ $\mu_{r,\,g\text{-}g} = \mu_{r,\,g\text{-}s} = 0.3$
○ $\mu_{r,\,g\text{-}g} = \mu_{r,\,g\text{-}s} = 0.4$
□ $\mu_{r,\,g\text{-}g} = \mu_{r,\,g\text{-}s} = 0.5$
△ $\mu_{r,\,g\text{-}g} = \mu_{r,\,g\text{-}s} = 0.6$
Experimental

Figure 13

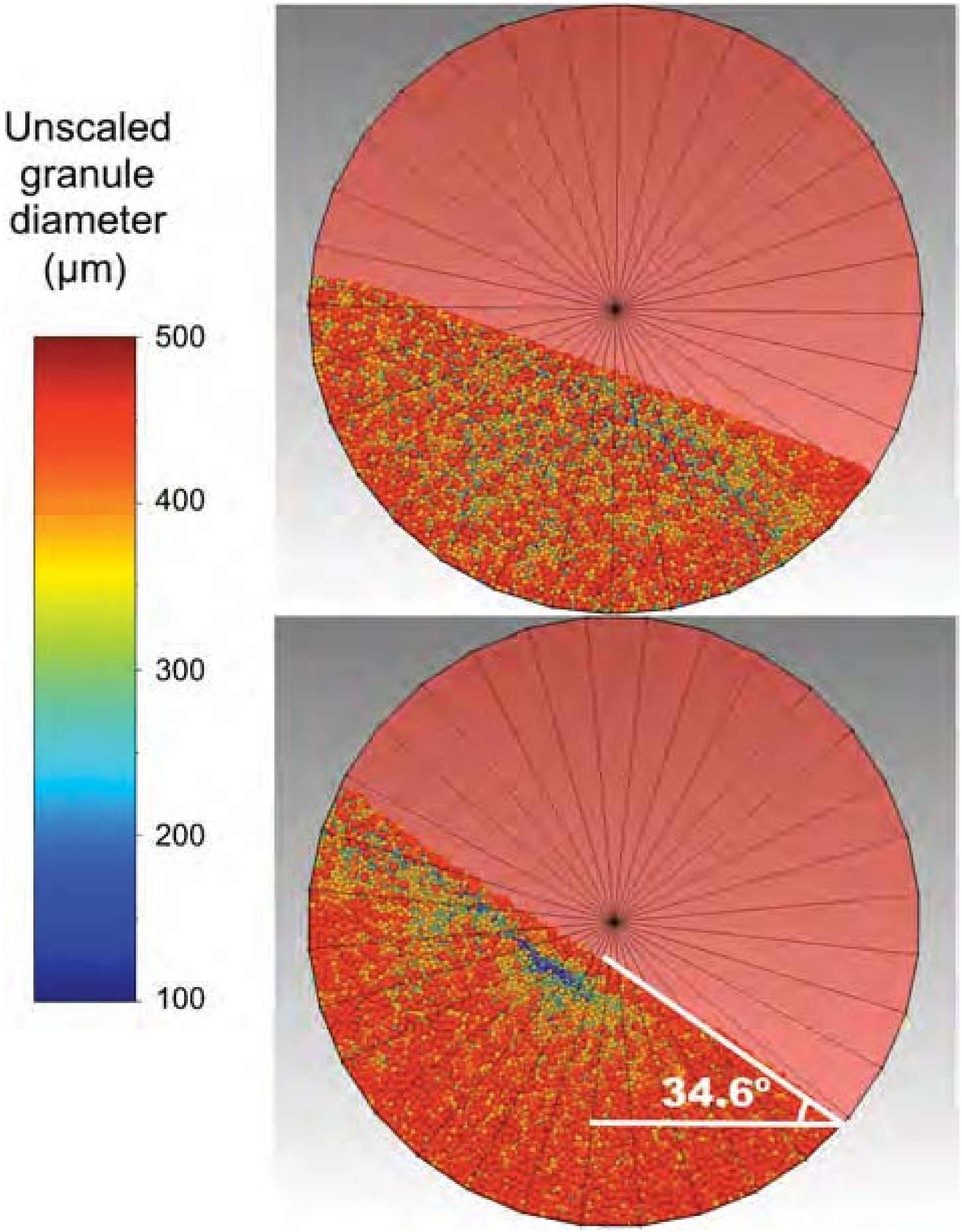

Figure 14

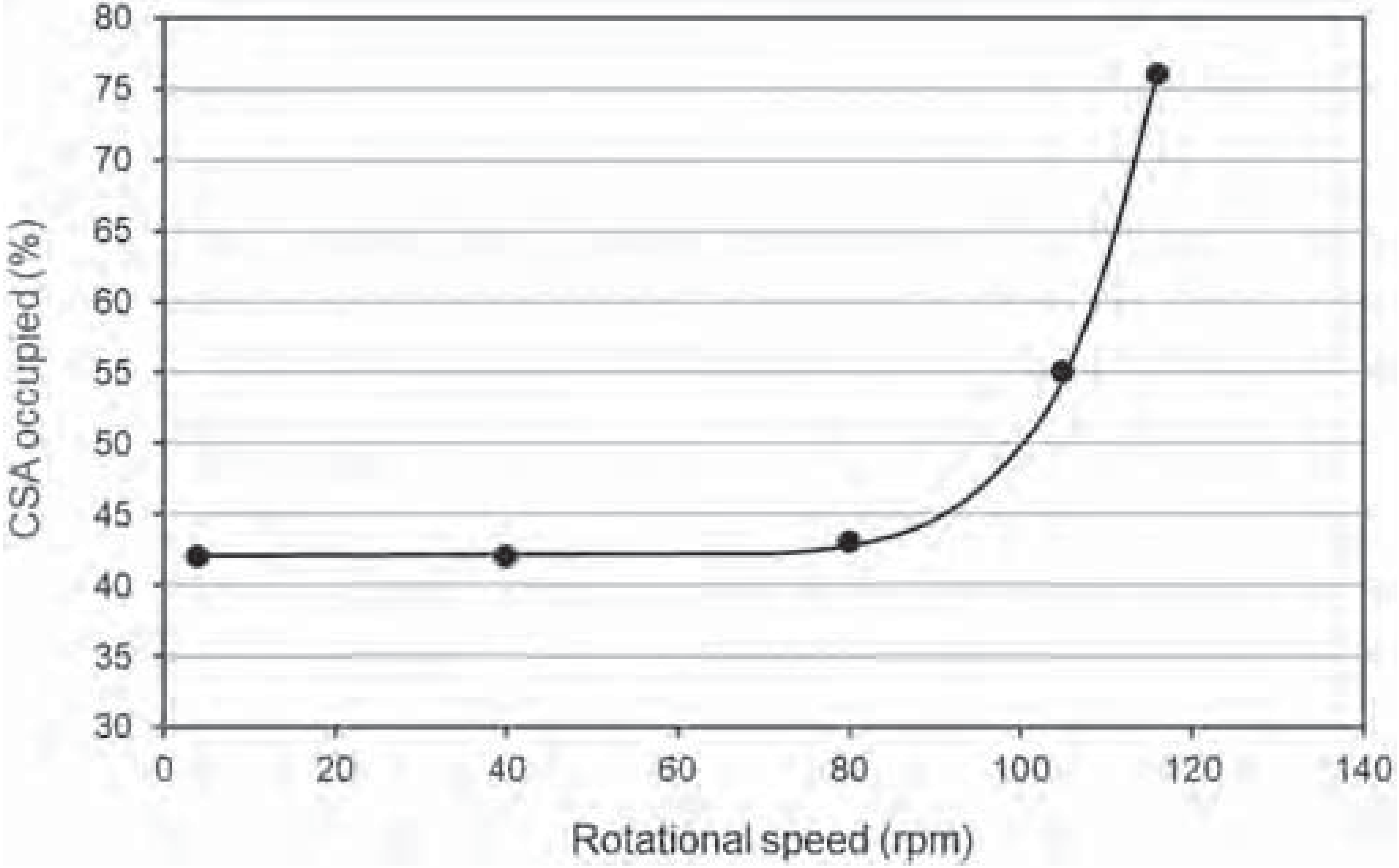
CSA occupied (%)
80
75
70
65
60
55
50
45
40
35
30
0
20
40
60
80
100
120
140
Rotational speed (rpm)

Figure 15

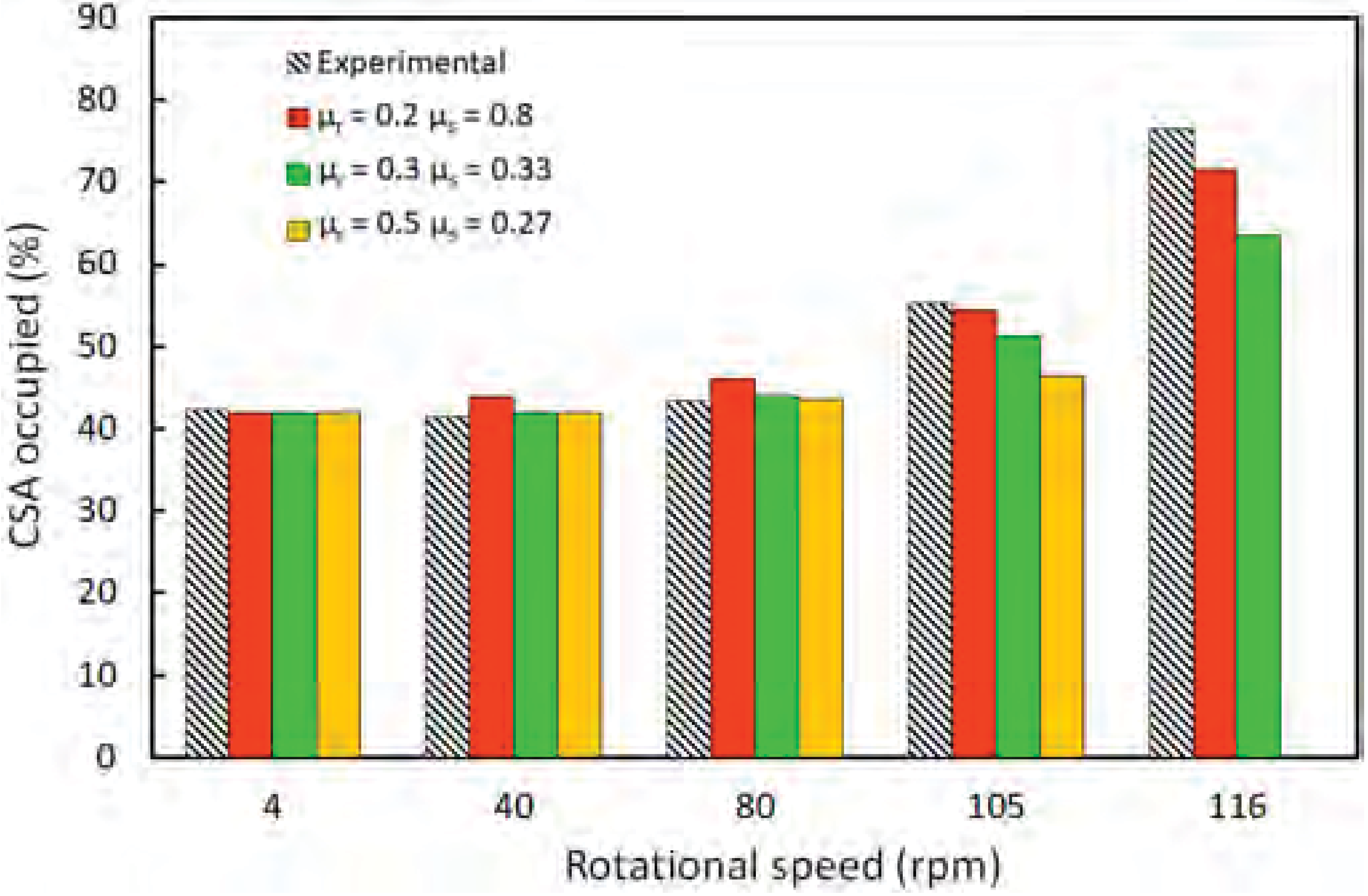

▨ Experimental
🟥 $\mu_r = 0.2$ $\mu_s = 0.8$
🟩 $\mu_r = 0.3$ $\mu_s = 0.33$
🟨 $\mu_r = 0.5$ $\mu_s = 0.27$
CSA occupied (%)
0
10
20
30
40
50
60
70
80
90
Rotational speed (rpm)
4
40
80
105
116

Figure 16

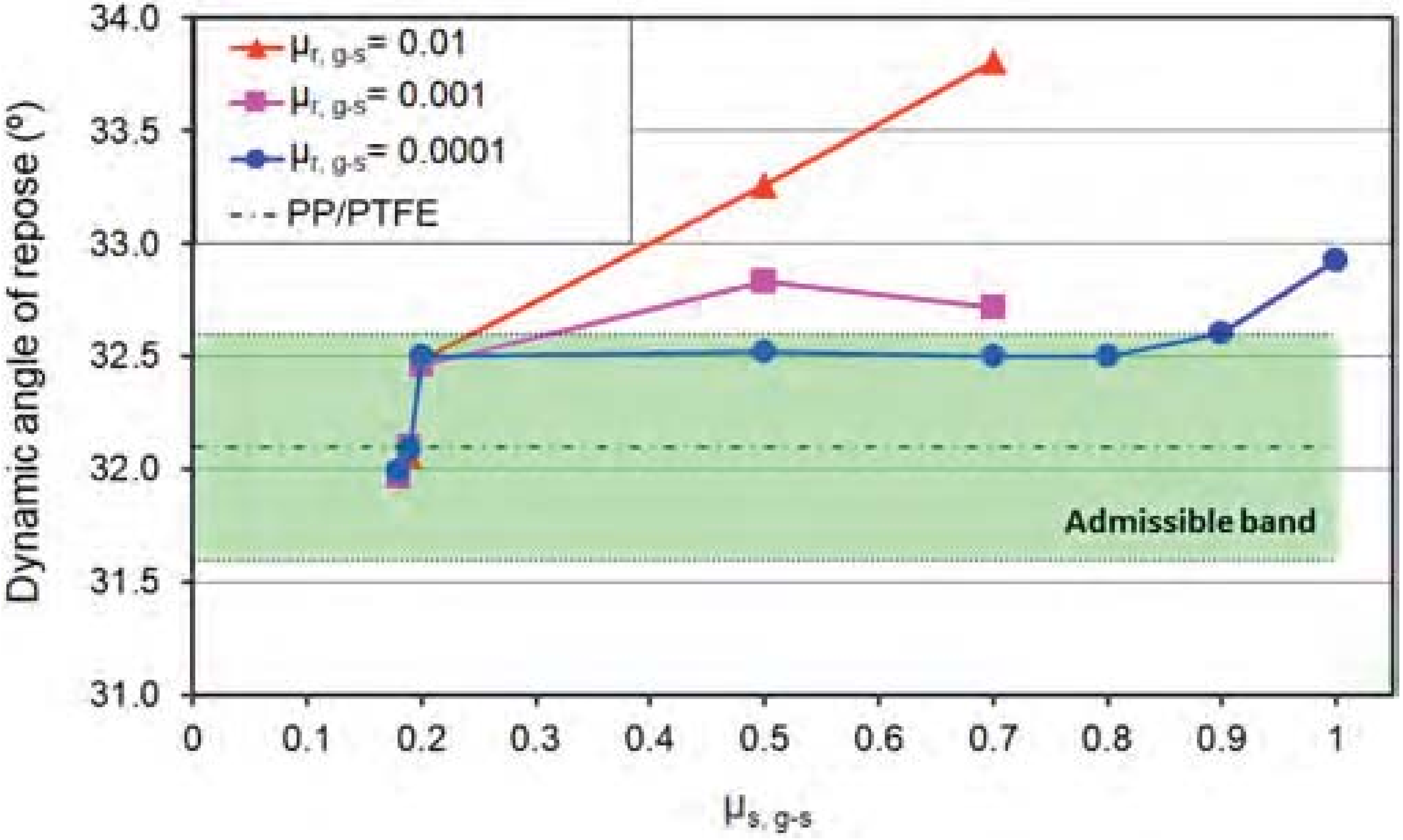
$\mu_{r,\,g\text{-}s}$= 0.01
$\mu_{r,\,g\text{-}s}$= 0.001
$\mu_{r,\,g\text{-}s}$= 0.0001
PP/PTFE
Admissible band
Dynamic angle of repose (°)
34.0
33.5
33.0
32.5
32.0
31.5
31.0
0
0.1
0.2
0.3
0.4
0.5
0.6
0.7
0.8
0.9
1
$\mu_{s,\,g\text{-}s}$

Figure 17

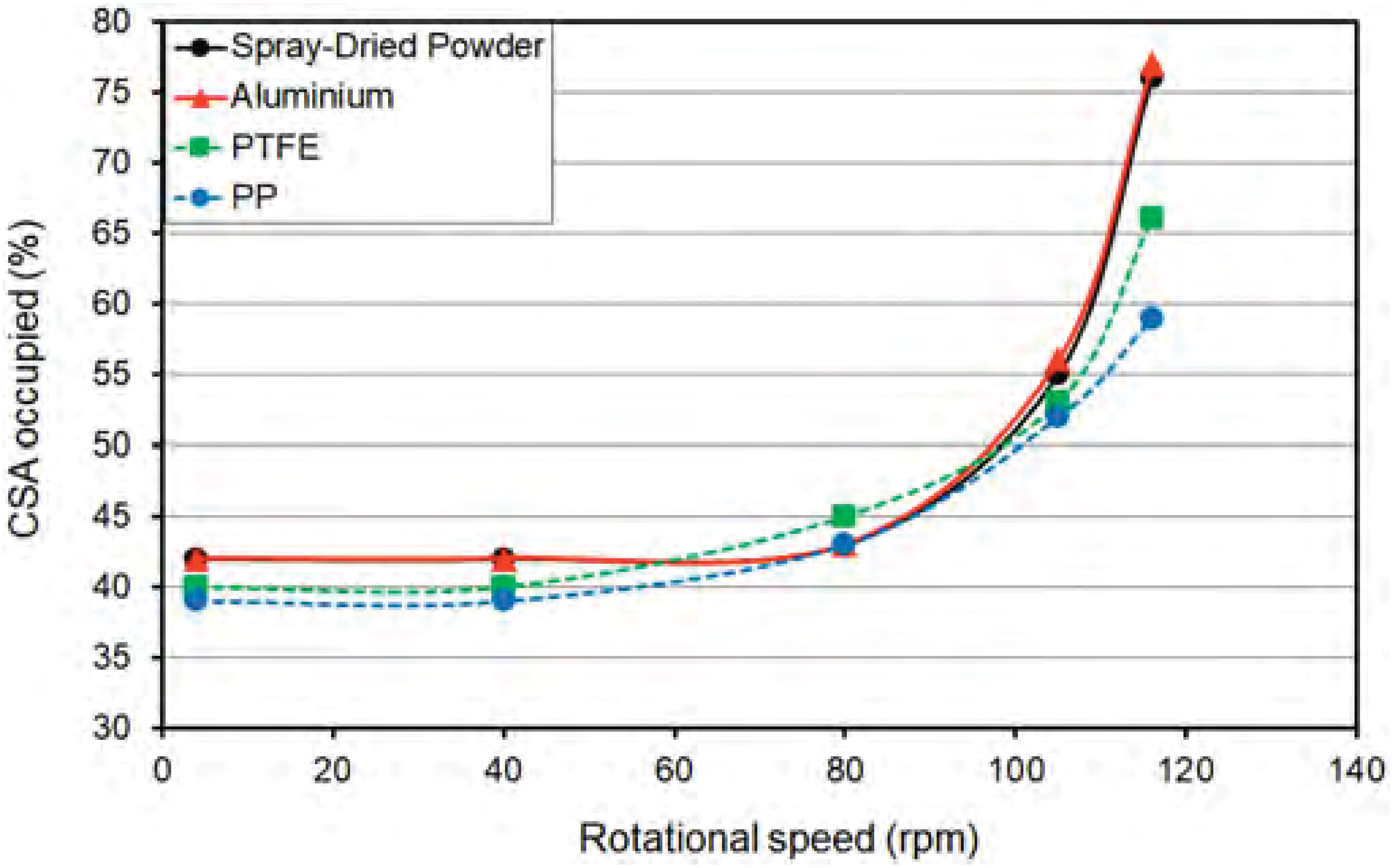
Spray-Dried Powder
Aluminium
PTFE
PP
CSA occupied (%)
80
75
70
65
60
55
50
45
40
35
30
0
20
40
60
80
100
120
140
Rotational speed (rpm)

Figure 18

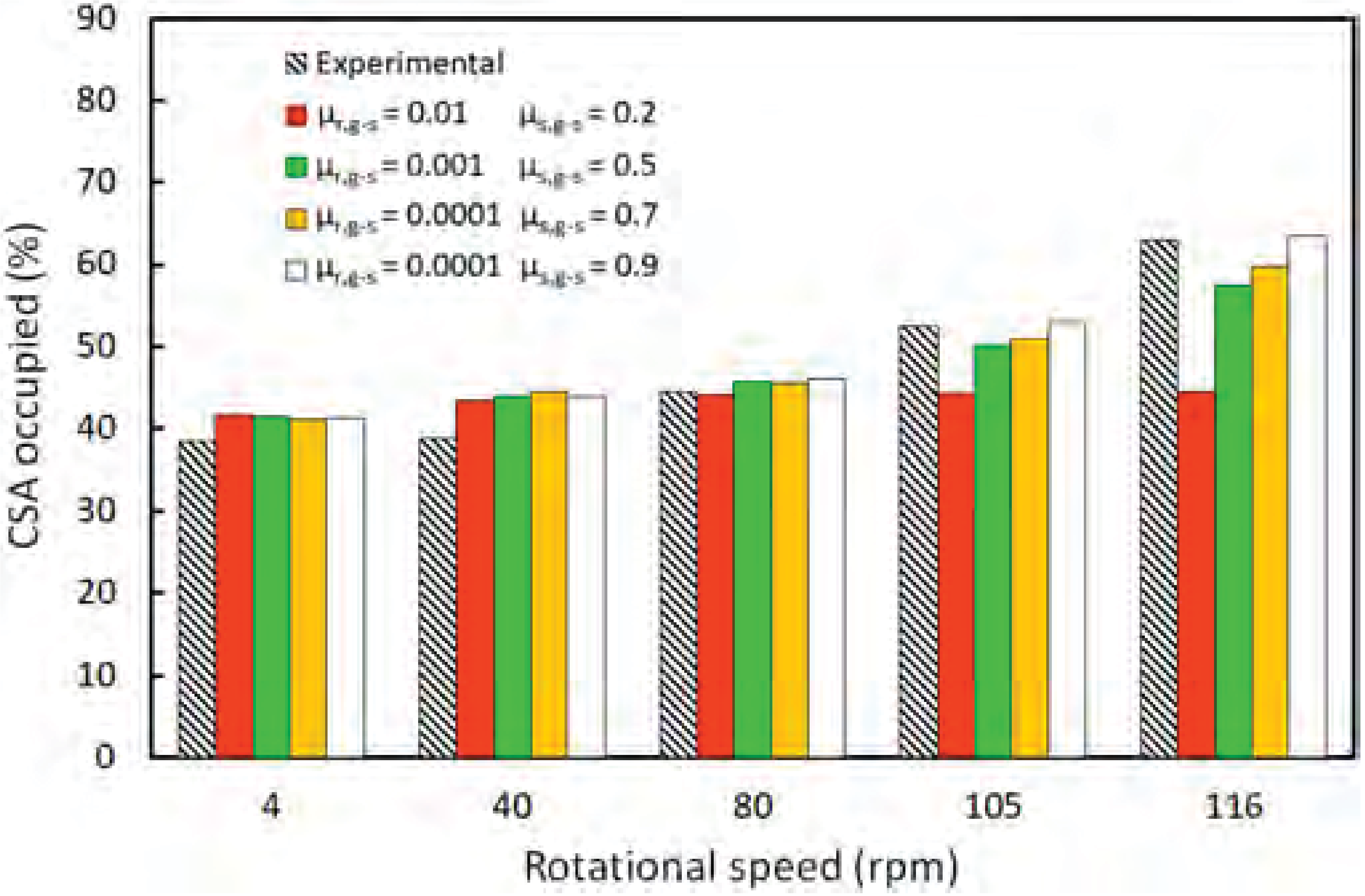
CSA occupied (%)
0
10
20
30
40
50
60
70
80
90
Experimental
$\mu_{r,g\text{-}s} = 0.01$ $\mu_{s,g\text{-}s} = 0.2$
$\mu_{r,g\text{-}s} = 0.001$ $\mu_{s,g\text{-}s} = 0.5$
$\mu_{r,g\text{-}s} = 0.0001$ $\mu_{s,g\text{-}s} = 0.7$
$\mu_{r,g\text{-}s} = 0.0001$ $\mu_{s,g\text{-}s} = 0.9$
4
40
80
105
116
Rotational speed (rpm)

Figure 19